



# DEM investigation on flow instability of particulate assemblies under coupling between volumetric and axial strains

M. Salimi<sup>1,2</sup> · A. Lashkari<sup>2</sup> · M. Tafili<sup>1</sup>

Received: 23 February 2023 / Accepted: 20 March 2024  
© The Author(s) 2024

## Abstract

The discrete element method (DEM) is employed to investigate the impact of coupling between volumetric and axial strains on the flow liquefaction vulnerability of 3D cubic particulate specimens. The virtual testing program conducted here encompasses a wide range of initial states and varying degrees of coupling between volumetric and axial strains. Utilizing data obtained from DEM simulations, the evolution of micro- and macroscale variables, including coordination number, contact fabric anisotropy, redundancy index, strong force networks, invariants of the effective stress tensor, and excess pore-water pressure, is examined. Results from DEM tests indicate that coupling expansive volumetric strain with axial strain leads to a gradual loosening of the load bearing microstructure, a decrease in coordination number, and a faster change in contact anisotropy. DEM simulations demonstrate that the triggering of flow liquefaction instability is followed by a sudden increase in contact fabric anisotropy and abrupt drops in coordination number and redundancy index. Moreover, a detailed analysis of the findings suggests that the stress ratio at the onset of post-peak softening decreases with increasing expansive volumetric strains.

**Keywords** Anisotropy · Coordination number · Critical state · DEM · Flow liquefaction · Volumetric strain

## 1 Introduction

Loose sands subjected to constant volume (undrained) conditions may exhibit flow instability, characterized by post-peak loss of shear strength, significant permanent shear deformations, and excessive accumulation of pore-water pressure (e.g., studies by Been and Jefferies [5], Chu et al. [9], and Chu and Wanatowski [11]). Laboratory findings have indicated that granular soil in a loose state, positioned above the critical state line (CSL) in the  $e$  versus  $p'$  plane, is particularly prone to flow instability.

Conversely, dense sand located below the CSL in this plane demonstrates continuous strain hardening without signs of flow instability.

Geotechnical design typically relies on strength parameters obtained from either fully drained or fully undrained tests. This approach is grounded in the belief that drained and undrained tests encapsulate the widest range of potential responses. However, real-world conditions seldom align with these extremes; instead, they tend to fall within a spectrum of partial drainage. This entails concurrent alterations in both pore volume and pore-water pressure. In particular, the traditional investigation of sand flow instability has focused on conventional tests such as constant volume triaxial, simple shear, and hollow cylinder torsion shear tests (e.g., [4, 8–11, 20, 31, 32, 36, 57, 60, 61, 69]). However, recent dynamic centrifuge studies have underscored the unrealistic nature of assuming negligible volume change (commonly referred to as undrained or isochoric conditions) in earthquake time scales due to void ratio redistribution caused by pore-water migration and soil heterogeneity (e.g., [1, 19, 41, 66]).

Instances where the assumption of negligible volume change does not hold, such as in the foundations of wind

---

✉ M. Salimi  
Mohammad.salimi@rub.de; Mj.salimi@sutech.ac.ir

A. Lashkari  
Lashkari@sutech.ac.ir

M. Tafili  
merita.tafili@rub.de

<sup>1</sup> Chair of Soil Mechanics, Foundation Engineering and Environmental Geotechnics, Ruhr-University Bochum, Bochum, Germany

<sup>2</sup> Department of Civil and Environmental Engineering, Shiraz University of Technology, Shiraz, Iran

turbines subjected to high cyclic loading from wind, waves, and storm forces, highlight the practical relevance of considering the coupling between volumetric and axial strains [2]. With the increasing development of offshore wind turbines, which feature shorter drainage paths compared to conventional gravity-based structures, there is a growing need to investigate this aspect of granular soil behavior [59]. To delve deeper into this phenomenon, researchers have devised specialized fully automated triaxial tests where controlled volume changes are imposed during shear, revealing that even small dilatative (expansive) volume changes can significantly intensify the potential for flow instability. Conversely, contractive volume changes tend to mitigate the susceptibility to flow instability (e.g., [24, 30, 45, 46, 56, 62]). More recent studies employing critical state-based constitutive models have corroborated these findings, showing that expansive volume changes resulting from pore-water inflow increase the potential for flow instability, while pore-water outflow weakens it (e.g., [18, 25, 30, 32, 60]).

In recent years, the discrete element method (DEM) introduced by Cundall and Strack [12] has demonstrated its unique ability as a versatile tool for synchronized investigation of the micro- as well as macroscale mechanical response of granular media (e.g., [7, 13, 15–17, 27, 34, 37, 38, 38, 40, 42, 44, 48, 50, 51, 53, 55, 58, 67, 68, 71]). For instance, in the simulation of drained and undrained tests carried out in the conventional and true triaxial apparatuses, clear correlations between asymptotic coordination number, invariants of various fabric tensors at the critical state, and invariants of the effective stress tensor have been reported in the literature (e.g., [13, 14, 16, 17, 33, 40, 43, 44, 50, 55, 67, 71]).

As aforementioned, during and after earthquakes, pore-water flux in sand elements can cause volume changes, impacting flow instability. The persistence of coupling between volumetric and shear strains prevents sand elements from reaching the critical state. Despite a few studies using DEM to investigate flow instability triggering [46, 50, 65], the literature lacks diverse coupled strain paths, and attention to micromechanical quantities.

Herein, 3D-DEM simulations are incorporated to investigate the influence of coupling between volumetric and axial strains on the flow instability of particulate assemblies. To this aim, this paper is organized as follows. Micro- and macroscale variables are introduced first. Then, the mechanical behaviors of 34 assemblies under uncoupled (i.e., 24 constant volume, and 28 drained) triaxial tests are simulated. Thereafter, impacts of linear and transient patterns of coupling between the volumetric and axial strains on mobilization of shear strength, effective stress path, variation of void ratio, accumulation of equivalent excess pore-water pressure, variation of coordination number, evolution

of anisotropy, and change in redundancy index are investigated. Through analyzing the data of a total of 213 simulations with coupling between the volumetric and axial strains, impacts of linear coupling coefficient, limiting volume change, and pace of volume change on stress ratio at the onset of post-peak softening are studied.

## 2 DEM modeling

### 2.1 Definition of macroscopic and microscopic variables

In this paper, for any arbitrary vectors  $\mathbf{a}$  and  $\mathbf{b}$ , tensor product of two vectors is  $\mathbf{a} \otimes \mathbf{b} = a_i b_j$ . For second-order tensors  $\mathbf{x}$  and  $\mathbf{y}$ ,  $\text{tr } \mathbf{x} = x_{ii}$  and  $\text{dev } \mathbf{x} = \mathbf{x} - [(1/3) \text{tr } \mathbf{x}] \mathbf{1}$  in which  $\mathbf{1}$  denotes the second-order identity tensor.  $\|\mathbf{x}\| = \sqrt{\mathbf{x} : \mathbf{x}}$  wherein  $\mathbf{x} : \mathbf{y} = x_{ij} y_{ij}$ .

An average granular stress tensor (i.e.,  $\boldsymbol{\sigma}$ ) on boundaries of a representative volume of a system consisting of a large number of discrete particles is [13, 14, 23, 50, 54, 71]:

$$\boldsymbol{\sigma} = \frac{1}{V} \sum_{c \in N_c} \mathbf{l}^c \otimes \mathbf{f}^c \quad (1)$$

wherein  $V$  and  $N_c$  are total volume and total number of contacts in the representative volume,  $\mathbf{l}^c$  is the branch vector connecting the centers of two contacting particles, and  $\mathbf{f}^c$  is the contact force at contact  $c$ . The first and second invariants of  $\boldsymbol{\sigma}$ , mean principal effective stress (i.e.,  $p'$ ) and shear stress (i.e.,  $q$ ), are:

$$p' = \frac{1}{3} \text{tr } \boldsymbol{\sigma}; q = \sqrt{\frac{3}{2}} \|\text{dev } \boldsymbol{\sigma}\| \quad (2)$$

For any cubic particulate assemblies, the second-rank strain tensor can be calculated from  $\varepsilon_{ij} = (\partial u_i / \partial X_j + \partial u_j / \partial X_i) / 2$  wherein  $\mathbf{u} [= (u_1 \ u_2 \ u_3)]$  represents displacement vector and  $X_i$  [with  $i \in \{1, 2, 3\}$ ] stands for coordination (see Fig. 1 for the coordination system). Herein, the normal strains are calculated based on displacements at the boundary walls of the cubic granular assembly:

$$\varepsilon_i = \frac{2 \Delta H_i}{H_0 + H_i} \text{ in which } i \in \{1, 2, 3\} \quad (3)$$

wherein  $H_0$  represents the initial dimensions of identical sides of the cubic specimen (see Fig. 1). In Eq. (3),  $\varepsilon_i$ ,  $H_i$ , and  $\Delta H_i$  [=  $H_0 - H_i$ ] stand, respectively, for normal strain, current dimension, and change in dimension of the cubic particulate specimen along  $i$ -axis.

Hence, the first and second invariants of strain tensor, the volumetric strain (i.e.,  $\varepsilon_v$ ) and the shear strain (i.e.,  $\varepsilon_q$ ), become [14, 50, 71]:

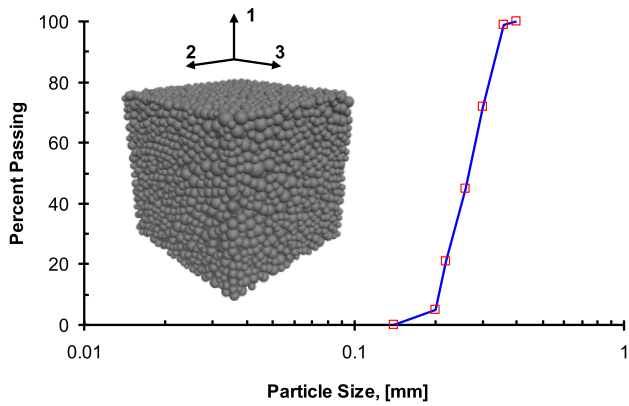


**Fig. 1** Particle size distribution used in preparation of DEM particulate assemblies and 3D view of a particulate assembly

$$\varepsilon_v = \frac{2\Delta V}{V_o + \Delta V}$$

$$\varepsilon_q = \sqrt{\frac{2}{3}} \|\text{dev } \boldsymbol{\varepsilon}\| = \frac{\sqrt{2}}{3} \sqrt{(\varepsilon_1 - \varepsilon_2)^2 + (\varepsilon_1 - \varepsilon_3)^2 + (\varepsilon_2 - \varepsilon_3)^2} \quad (4)$$

A second-order fabric tensor (i.e.,  $\mathbf{F}$ ) is adopted to characterize the evolving contact anisotropy in assemblies of discrete spheres [14, 22, 23, 26, 37, 38, 43, 44, 50, 52, 71]:

$$\mathbf{F} = \frac{1}{N_c} \sum_{k=1}^{N_c} \mathbf{n}^k \otimes \mathbf{n}^k \quad (5)$$

wherein  $\mathbf{n}^k$  is unit vector normal to the  $k$ th contact plane. The second invariant of  $\mathbf{F}$ , i.e.,  $\text{dev } \mathbf{F} [= \mathbf{F} - (\text{tr} \mathbf{F}/3)\mathbf{1}]$ , is frequently used as a scalar measure of anisotropy in granular media [14, 39, 43, 50, 52, 70]:

$$\|\text{dev } \mathbf{F}\| = \sqrt{\text{dev } \mathbf{F} : \text{dev } \mathbf{F}} = \sqrt{\mathbf{F} : \mathbf{F} - \frac{1}{3}(\text{tr } \mathbf{F})^2} \quad (6)$$

The coordination number (CN), the average contact number per particle, is an appropriate index of mechanical stability in particulate systems [14, 34, 42, 48]:

$$\text{CN} = \frac{2N_c}{N_p} \quad (7)$$

wherein  $N_p$  and  $N_c$  are, respectively, the total number of particles and total number of contacts in the representative volume  $V$ . A contact commences once two particles touch each other, and accordingly,  $N_c$  was multiplied by 2 in Eq. (7).

In 3D assemblies of discrete particles, the total number of elastic constrains associated with  $N_c$  contacts is  $(3 - 2f_s)N_c$  wherein  $f_s$  is the ratio of total sliding (say plastic) contacts to the total number of contacts of note, in a sliding contact, the mobilized tangential contact force reached its

ultimate value which is dictated by both the normal force and inter particle friction angle,  $\mu$ , at the contact point. On the other hand,  $6N_p$  degrees of freedom exist for 3D assemblies of  $N_p$  discrete particles. Excluding particles with zero active contacts (i.e.,  $N_p^0$ ), Kruyt and Rothenburg [28], Zhou et al. [71] and Huang et al. [17] suggested redundancy index (i.e.,  $I_R$ ) in terms of the ratio of the total number of constraints to the total number of degrees of freedom in particulate assembly:

$$I_R = \left(\frac{3 - 2f_s}{6}\right) \frac{N_c}{N_p - N_p^0} = \left(\frac{3 - 2f_s}{12}\right) \frac{\text{CN}}{1 - (N_p^0/N_p)} \quad (8)$$

A transition from  $I_R > 1$  to  $I_R < 1$  points to a shift from situations in which the total number of constraints are higher than the total degrees of freedom (say hyperstatic regime) to other situations wherein the total number of constraints is lower than the total degrees of freedom (say hypostatic regime). Accordingly, assemblies with  $I_R < 1$  are potentially unstable and  $I_R = 1$  can be considered as the onset of instability.

### 2.2 Specimen preparation

The DEM simulations have been executed using the commercial code PFC3D [21]. The mathematical foundation of DEM can be found in Cundall & Strack [12]. The adopted particle size distribution for the particulate assemblies of this study is shown in Fig. 1. The specimen preparation scheme suggested by Gu et al. [13] was followed; that is, specimens with a total of 8438 spherical particles were first generated in a 5[mm] × 5[mm] × 5[mm] inner cubic space between orthogonal boundary walls for imposing external forces and displacements. A cloud of randomly distributed particles was initially positioned in the inner space between boundary walls. Then, among different existing rules for particle–particle and particle–wall interactions, the one with linear force–displacement contact law was employed. Afterward, the interparticle friction coefficient (denoted as  $\mu$ ) is set to zero, and the particles undergo cycling until they attain a mechanical ratio of  $10^{-5}$ . This ratio is calculated as the average value of the unbalanced force magnitude divided by the average value of the sum of the magnitudes of the contact forces. Imposing equal inward movement of walls, an isotropic stress state with confining stress of 10 [kPa] was imposed on the specimens. To generate specimens with a wide range of initial void ratios, relatively large  $\mu$  values (i.e., 0.7–1.0 [-]) during this stage led to the generation of loose specimens, whereas dense specimens were produced via facilitation of particles sliding through assuming low  $\mu$  values (e.g., 0.05–0.3 [-]). Thereafter,  $\mu$  was set to 0.5 [-] and each specimen was brought to its prescribed target

confining stress (greater than 10 [kPa]) and cycled once more to reach equilibrium. To ensure the rigidity of wall boundaries, the value of wall stiffness was chosen to be higher than particle stiffness. The parameters used in simulations are listed in Table 1. Table 2 provides a comprehensive list of the initial samples utilized in the simulations, along with their corresponding interparticle friction angles. In the preparation stage (confining stress of 10 [kPa]), varying friction angles were intentionally utilized to generate diverse initial sample configurations. However, minor fluctuations in void ratio are anticipated due to the dynamic interaction of particles, wherein some contacts remain stationary, creating spaces for smaller particles to fill.

### 3 Coupling of strains

#### 3.1 Mathematical definition

Two different patterns for coupling between the volumetric and axial strains, i.e., “linear” and “transient”, are considered here. In the linear pattern, the volumetric strain increases linearly with the axial strain through:

$$\varepsilon_v = \zeta \varepsilon_1 \quad (9)$$

wherein  $\varepsilon_1 (> 0)$  is normal strain along the 1-axis in Fig. 1 and  $\zeta$  is the proportionality factor.  $\zeta > 0$  corresponds to contractive (say  $\varepsilon_v > 0$ ) coupling with continuously decreasing void ratio per  $\varepsilon_1$  and  $\zeta < 0$  refers to expansive (say  $\varepsilon_v < 0$ ) coupling wherein void ratio increases constantly with  $\varepsilon_1$ . Of note,  $\zeta = 0$  dictates the constant volume (i.e., isochoric or undrained) condition.

In practical applications, several factors exert physical limitations on the maximum achievable volumetric strain. These factors encompass soil heterogeneity, the confined

extent of the liquefied zone, and the prevailing field drainage conditions. The behavior of volumetric strain exhibits a range of diverse patterns. In certain scenarios, it showcases a linear correlation with axial strain, while in others, it experiences nonlinear variations before eventually stabilizing at a constant volume state. This nonlinearity arises due to the inherent nature of filter boundaries, as they allow water to pass in proportion to the incremental pressure changes. Experimental evidence by Suzuki et al. [59] substantiates that the coupling between volumetric and axial strain induces nonlinear alterations in volumetric strain, which eventually reach a constant value as axial strain increases. The observed variability in this behavior can be influenced by two key factors: the rate of change in volumetric strain ( $R$ ), which is contingent upon filter permeability and the rate of loading, and the ultimate magnitude of volumetric strain ( $\varepsilon_{v\infty}$ ), representing the final volumetric strain state. Therefore, an idealized strain path with transient  $\varepsilon_v$ - $\varepsilon_1$  coupling leading to a limited volumetric strain is utilized here as follows:

$$\varepsilon_v = \varepsilon_{v\infty} [1 - \exp(-R\varepsilon_1)] \quad (10)$$

in which  $R$  is a positive parameter controlling the pace of  $\varepsilon_v$  with  $\varepsilon_1 (> 0)$  and  $\varepsilon_{v\infty}$  is the ultimate (i.e., limiting) volumetric strain at extremely large axial strains [say  $\varepsilon_1 \rightarrow +\infty$ ]. In Eq. (10),  $\varepsilon_{v\infty} > 0$  causes a contractive transient  $\varepsilon_v$ - $\varepsilon_1$  coupling, whereas  $\varepsilon_{v\infty} < 0$  refers to expansive transient  $\varepsilon_v$ - $\varepsilon_1$  coupling. The slope of the  $\varepsilon_v$  versus  $\varepsilon_1$  curve (i.e.,  $\partial\varepsilon_v/\partial\varepsilon_1$ ) from Eq. (10) begins from  $R\varepsilon_{v\infty}$  at  $\varepsilon_1 = 0$  and gradually approaches zero (i.e., undrained condition) as  $\varepsilon_1$  becomes very large. Typical curves visualizing the linear and transient  $\varepsilon_v$ - $\varepsilon_1$  couplings are, respectively, illustrated in parts “a” and “b” of Fig. 2.

#### 3.2 Consequence of $\varepsilon_v$ - $\varepsilon_1$ coupling: an energy-based interpretation

Adopting a minimum active to passive energy ratio criterion, Rowe [49] obtained a stress-dilation law for assemblies of unbreakable frictional particles sheared under triaxial compression (TXC) condition:

$$\frac{\sigma'_1}{\sigma'_3} = \tan^2\left(\frac{\pi}{4} + \frac{\phi'_{cs}}{2}\right) \left(1 - \frac{\dot{\varepsilon}_v}{\dot{\varepsilon}_1}\right) \quad (11)$$

wherein  $\sigma'_1$  and  $\sigma'_3$  are, respectively, the major (along the 1-axis in Fig. 1) and minor (along the 3-axis in Fig. 1) principal effective stresses, and  $\phi'_{cs}$  is the critical state friction angle. Recalling that  $\sigma'_1 = p' + (2/3)q$ ,  $\sigma'_3 = p' - (1/3)q$ , and  $\sin\phi'_{cs} = 3M/(6+M)$  [of note,  $M$  is slope of the CSL in the  $q$ - $p'$  plane] hold in TXC shear, rearrangement of terms in Eq. (11) with some ordinary algebra operations lead to the following equation for mobilization of stress ratio (i.e.,  $\eta$ ) with  $\dot{\varepsilon}_v/\dot{\varepsilon}_1$ :

**Table 1** Parameters used in DEM simulations in shearing stage

Parameter	Value
Particles density	2650 [kg/m <sup>3</sup> ]
Coefficient of interparticle friction	0.5 [–]
Particle–wall coefficient of friction	0.0 [–]
Wall stiffness	$1 \times 10^7$ [kN/m]
Particle normal stiffness ( $k_n$ )	$k_n = k_0 \times r$ wherein $k_0 = 1 \times 10^5$ [kN/m <sup>2</sup> ] and $r$ is particle radius
Particle normal stiffness ( $k_t$ )	$k_t = k_0 \times r$ wherein $k_0 = 1 \times 10^5$ [kN/m <sup>2</sup> ] and $r$ is particle radius
Damping constant	0.70 [–]

**Table 2** Initial data of samples and interparticle friction angles at different stages of preparation

Sample name	Friction during sample preparation ( $p = 10$ [kPa])	$e$ (at 10 [kPa])	CN (at 10 [kPa])	$\ \text{dev } \mathbf{F}\ $ (at 10 [kPa])	Friction in compaction and shearing stage	$p_0$ [kPa]	$e_0$ [-]	CN <sub>0</sub> [-]	$\ \text{dev } \mathbf{F}\ $	$e_{cs}$ [-]	$\psi_0$
A-1	0.00	0.598	5.950	0.0013	0.50	100	0.582	6.270	0.0017	0.722	- 0.140
A-2	0.00				0.50	200	0.565	6.483	0.0019	0.703	- 0.138
A-3	0.00				0.50	300	0.550	6.689	0.0021	0.684	- 0.134
A-4	0.00				0.50	600	0.507	7.088	0.0009	0.628	- 0.120
A-5	0.05	0.648	5.343	0.0013	0.50	100	0.629	5.824	0.0012	0.715	- 0.086
A-6	0.05				0.50	300	0.593	6.275	0.0003	0.684	- 0.091
A-7	0.05				0.50	600	0.546	6.690	0.0006	0.608	- 0.063
A-8	0.10	0.672	4.932	0.0020	0.50	200	0.632	5.874	0.0012	0.703	- 0.071
A-9	0.10				0.50	400	0.596	6.273	0.0005	0.665	- 0.069
A-10	0.15	0.689	4.712	0.0059	0.50	400	0.607	6.137	0.0035	0.665	- 0.058
A-11	0.15				0.50	300	0.626	5.936	0.0025	0.684	- 0.058
A-12	0.15				0.50	200	0.646	0.646	0.0037	0.703	- 0.057
A-13	0.15				0.50	50	0.679	5.205	0.0051	0.731	- 0.052
A-14	0.15				0.50	100	0.667	5.441	0.0043	0.722	- 0.055
A-15	0.20	0.700	4.513	0.0029	0.50	300	0.634	5.865	0.0040	0.684	- 0.050
A-16	0.20				0.50	100	0.677	5.301	0.0013	0.722	- 0.045
A-17	0.35	0.717	4.074	0.0038	0.50	100	0.691	5.045	0.0022	0.637	0.054
A-18	0.45	0.725	3.924	0.0008	0.50	200	0.671	5.354	0.0023	0.683	- 0.011
A-19	0.70	0.737	3.661	0.0044	0.50	600	0.594	6.142	0.0040	0.628	- 0.034
A-20	0.75	0.736	3.657	0.0036	0.50	100	0.703	4.775	0.0049	0.721	- 0.018
A-21	0.75				0.50	50	0.719	4.370	0.0023	0.731	- 0.012
A-22	0.80	0.735	3.631	0.0037	0.50	100	0.701	4.773	0.0062	0.715	- 0.014
A-23	0.85	0.738	3.622	0.0035	0.50	100	0.704	4.738	0.0025	0.715	- 0.011
A-24	0.90	0.737	3.532	0.0031	0.50	50	0.718	4.302	0.0030	0.731	- 0.013
A-25	0.90				0.50	100	0.718	4.302	0.0030	0.715	0.003
A-26	0.95	0.740	3.586	0.0029	0.50	20	0.729	3.908	0.0051	0.735	- 0.006
A-27	0.95				0.50	35	0.724	4.134	0.0048	0.731	- 0.007
A-28	0.95	0.740	3.586	0.0029	0.50	200	0.678	5.191	0.0012	0.703	- 0.025
A-29	1.00	0.742	3.555	0.0062	0.50	400	0.633	5.758	0.0037	0.665	- 0.032
A-30	1.00				0.50	300	0.655	5.514	0.0033	0.645	0.010
A-31	1.00				0.50	100	0.706	4.696	0.0037	0.715	- 0.009
A-32	1.00				0.50	75	0.713	4.500	0.0033	0.705	0.008
A-33	1.00				0.50	50	0.720	4.279	0.0033	0.728	- 0.007
A-34	1.00				0.50	200	0.679	5.166	0.0032	0.690	- 0.011

$$\eta = \frac{q}{p'} = 3 \frac{\left(\frac{\sigma'_1}{\sigma'_3} - 1\right)}{\left(\frac{\sigma'_1}{\sigma'_3} + 2\right)} = \frac{M - \left(1 + \frac{2}{3}M\right) \left(\frac{\dot{\varepsilon}_v}{\dot{\varepsilon}_1}\right)}{1 - \frac{1}{3} \left(1 + \frac{2}{3}M\right) \left(\frac{\dot{\varepsilon}_v}{\dot{\varepsilon}_1}\right)} \quad (12)$$

Equation (12) signifies that  $\dot{\varepsilon}_v/\dot{\varepsilon}_1$ , commonly referred as dilation in the soil mechanics literature (e.g., Bolton [6]), plays a central role in mobilization of  $\eta$  in the unbreakable frictional granular soils under shear. Following treatments of Wan and Guo [63] and Li and Dafalias [35],  $M$  may be replaced by either  $M^* = M(e/e_{cs})^\theta$  or  $M^* = M \exp(m\psi)$ , respectively, in order to further refine predictive capacity

of Eq. (12) for granular media of dissimilar states with respect to the CSL wherein  $\theta$  and  $m$  are positive material parameters.  $e$  and  $e_{cs}$  are the current and critical state void ratios and  $\psi = e - e_{cs}$  is the state parameter of Been and Jefferies [4].

For the conventional drained tests wherein  $\varepsilon_v$  and  $\varepsilon_1$  are uncoupled ( $\varepsilon_1$  is applied and  $\varepsilon_v$  is the free response of soil specimen),  $\varepsilon_v$  is nullified gradually and simultaneously,  $\eta$  approaches toward  $M$  with the increase in  $\varepsilon_1$  [say  $(\dot{\varepsilon}_v/\dot{\varepsilon}_1) \rightarrow 0$ ,  $\eta \rightarrow M$  and  $e \rightarrow e_{cs}$  (equally  $\psi \rightarrow 0$ ) as  $\varepsilon_1 \rightarrow +\infty$ ]. For the linear



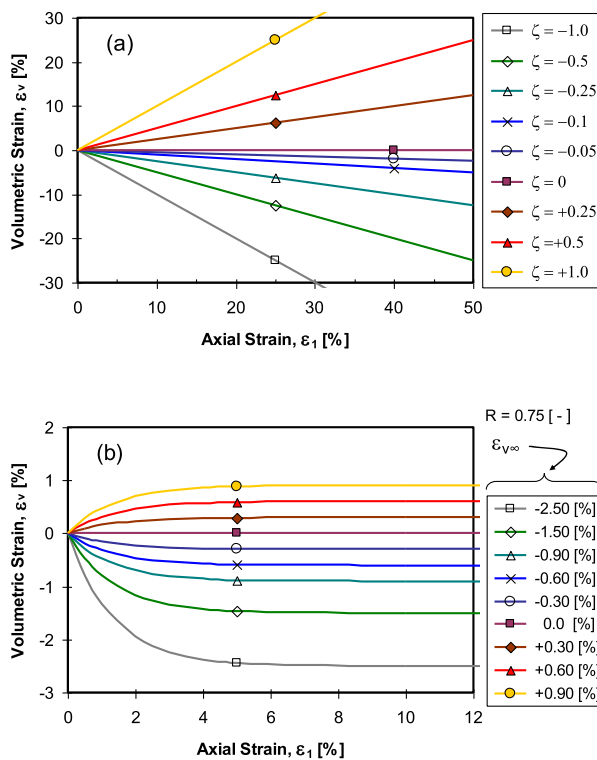


**Fig. 2** Typical strain paths studied here: **a** linear  $\varepsilon_v - \varepsilon_1$  coupling with  $\zeta = -1.0, -0.50, -0.25, -0.10, -0.05, 0.0, +0.25, +0.50,$  and  $+1.0$ ; and **b** transient  $\varepsilon_v - \varepsilon_1$  coupling with  $R = 0.75$  and  $\varepsilon_{v\infty} = -2.50, -1.50, -0.90, -0.60, -0.30, 0, +0.30, +0.60,$  and  $+0.90$  [%]

$\varepsilon_v - \varepsilon_1$  coupling (see Eq. (9)),  $\dot{\varepsilon}_v / \dot{\varepsilon}_1 [= \zeta]$  is kept fixed during shear, and thus,  $\eta$  approaches steadily to  $[M^* - \zeta(1 + 2M^*/3)] / [1 - \zeta(1 + 2M^*/3)/3]$  as  $\varepsilon_1 \rightarrow +\infty$ . This means that  $\eta$  does not approach  $M$  and the critical state is not achieved owing to the linear  $\varepsilon_v - \varepsilon_1$  coupling unless  $\zeta = 0$  [i.e., constant volume condition] is prescribed. Under the constant volume condition,  $e \rightarrow e_{cs}$  (say  $\psi \rightarrow 0$ ),  $M^* \rightarrow M$ , and accordingly,  $\eta \rightarrow M$  happen as  $\varepsilon_1 \rightarrow +\infty$ . Differentiation of Eq. (10) yields  $(\dot{\varepsilon}_v / \dot{\varepsilon}_1) = R(\varepsilon_{v\infty} - \varepsilon_v)$ , and accordingly,  $\eta$  is calculated from  $[M^* - R(\varepsilon_{v\infty} - \varepsilon_v)(1 + 2M^*/3)] / [1 - R(\varepsilon_{v\infty} - \varepsilon_v)(1 + 2M^*/3)/3]$  for the transient  $\varepsilon_v - \varepsilon_1$  coupling. In this case, the critical state is achieved asymptotically as  $\varepsilon_v \rightarrow \varepsilon_{v\infty}$ . Based on these, it can be concluded that  $\varepsilon_v - \varepsilon_1$  coupling can prevent [under linear coupling] or cause a major delay [under transient coupling] in reaching the actual critical state in granular media. Therefore, the critical state frame is adopted in the following sections as a benchmark. The macro- and microscale responses of particulate assemblies sheared under linear and transient  $\varepsilon_v - \varepsilon_1$  coupling are then compared to those attained from identical assemblies sheared under the constant volume condition in the critical state frame.

## 4 Macro- and microscale behavior

### 4.1 Uncoupled TXC paths

Been and Jefferies [5] put forward evidence for a strong connection between sand behavior and initial state parameter (i.e.,  $\psi_0$ ):

$$\psi_0 = e_0 - e_{cs} \quad (13)$$

wherein  $e_0$  and  $e_{cs}$  are the initial and critical state void ratios, respectively. Sands are in dense state and exhibit non-flow strain hardening when  $\psi_0 < \psi_{lim}$  (in which  $\psi_{lim} = -0.05$  to zero), whereas loose sands with  $\psi_0 > \psi_{lim}$  have a tendency to post-peak softening and flow instability under constant volume (undrained) shear. Values for  $e_0$ ,  $e_{cs}$ , and  $\psi_0$  are reported in Table 2 and final state parameters of drained and undrained tests reported in Table S1 (see supplementary materials).

The constant volume behavior of four dense ( $\psi_0 = -0.033$  to  $-0.136$ ) assemblies exhibits non-flow strain-hardening behavior up to a reasonably unique critical state in the  $q$  versus  $p'$  [Fig. 3a] and  $q$  versus  $\varepsilon_q$  [Fig. 3b] planes. In Fig. 3c, CN for the specimens with  $p'_c = 400$  and  $600$  [kPa] descends steadily with  $\varepsilon_q$  from  $6.25$  and  $6.15$  at  $\varepsilon_q = 0$  toward  $CN_{cs} \approx 5.5$  at the end of the simulations. For the specimen with  $p'_c = 50$  and  $300$  [kPa], CN passes transient minimums at  $\varepsilon_q \approx 2.25$  [%] and  $7.25$  [%], respectively, and then improves gradually to reach  $CN_{cs} \approx 5.5$  [-] asymptotically.  $\|dev \mathbf{F}\|$  versus  $\varepsilon_q$  curves in Fig. 3d indicate that the decrease in  $\psi_0$  amplifies the peak in  $\|dev \mathbf{F}\|$ ; however, all  $\|dev \mathbf{F}\|$  versus  $\varepsilon_q$  curves approach gradually toward a unique  $\|dev \mathbf{F}\|_{cs} \approx 0.088$  [-] at large shear strains.

For three loose ( $\psi_0 = -0.012$  to  $-0.018$ ) assemblies sheared under the constant volume condition in Fig. 4a, b, flow instability triggered within the range  $\varepsilon_q \approx 1.0$ – $1.75$  [%], and thereafter, temporary minimum post-peak shear strengths were attained around  $\varepsilon_q \approx 6.0$ – $7.25$  [%] beyond which the  $q$  versus  $\varepsilon_q$  curves improved with  $\varepsilon_q$ . Due to insufficient shear in Fig. 4a,  $q$  did not become plateau prior to the end of simulations, and thus, none of the tests reached the actual critical state. Flow instability of loose sands triggers once the effective stress path intersects instability line obtained from connecting the origin of the  $q$  versus  $p'$  plane to the transient constant volume peak shear strength [2, 3, 11, 29, 30, 57, 64]. In Fig. 4b,  $\eta_{IL} \approx 0.50$  is attained for the slope of the instability line. Temporary minimums for CN in Fig. 4c happened around  $\varepsilon_q \approx 6.0$ – $8.5$  [%], and thereafter, CN improved with  $\varepsilon_q$ . Contrary to that for the dense assemblies in Fig. 3d,  $\|dev \mathbf{F}\|$  versus  $\varepsilon_q$  curves for the loose assemblies in Fig. 4d did not possess any concrete peak and they gradually rose with  $\varepsilon_q$  to reach

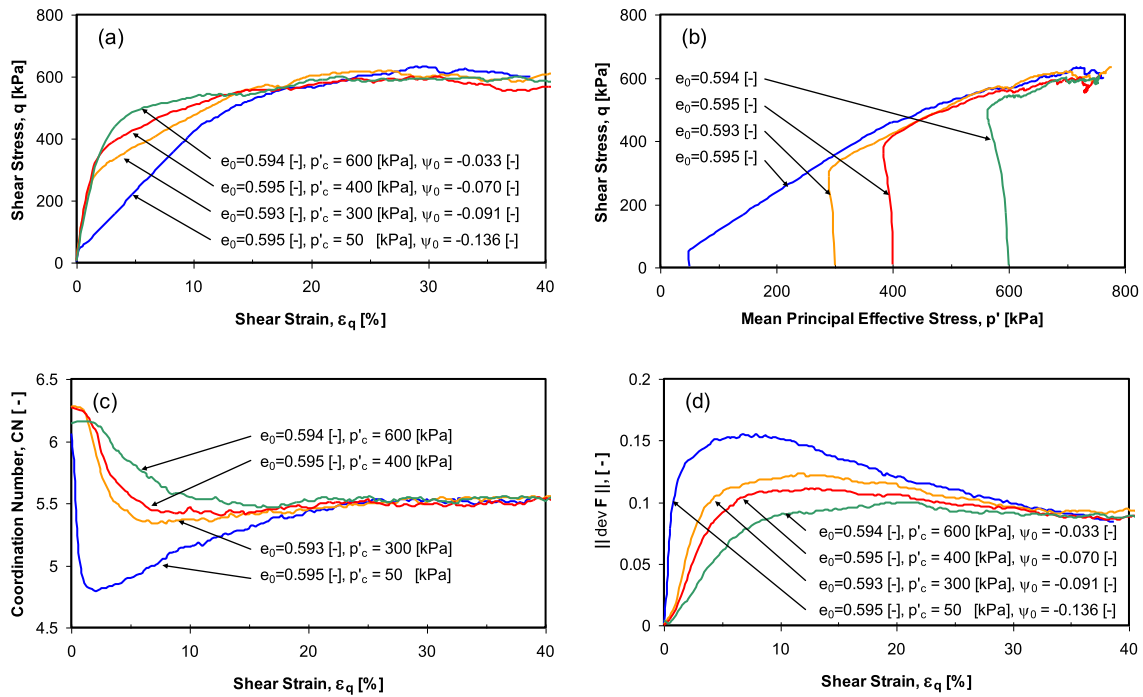


Fig. 3 Simulations for the constant volume TXC behavior of four dense particulate assemblies: **a**  $q$  versus  $\epsilon_q$ ; **b**  $q$  versus  $p'$ ; **c** CN versus  $\epsilon_q$ ; and **d**  $\|dev \mathbf{F}\|$  versus  $\epsilon_q$

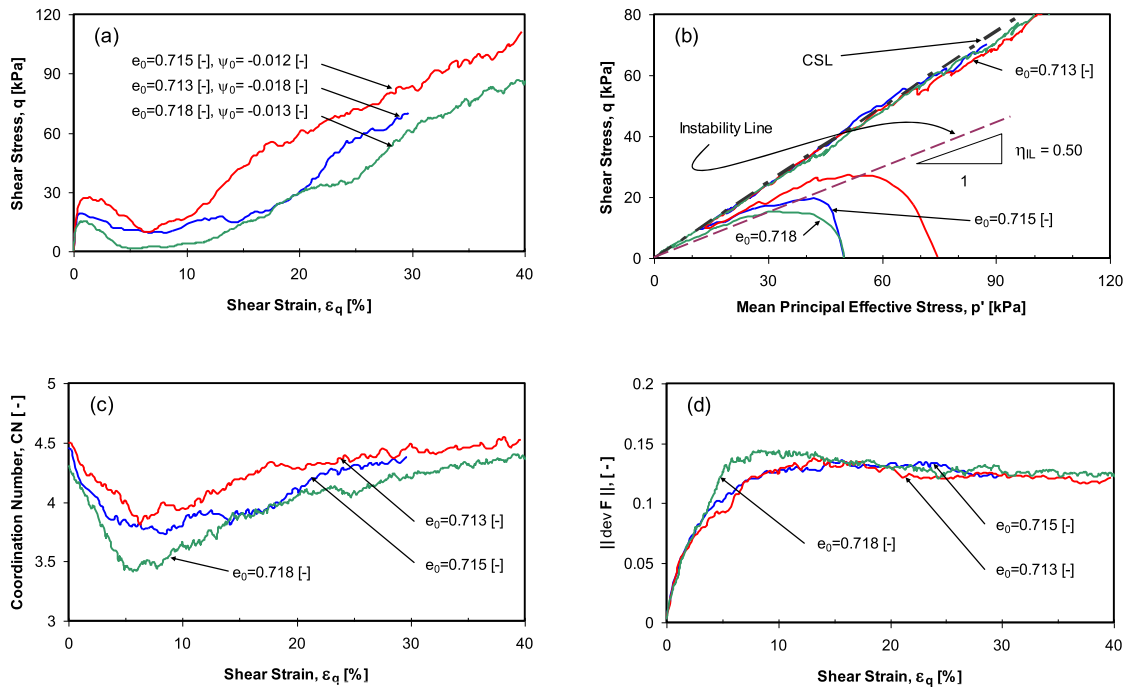
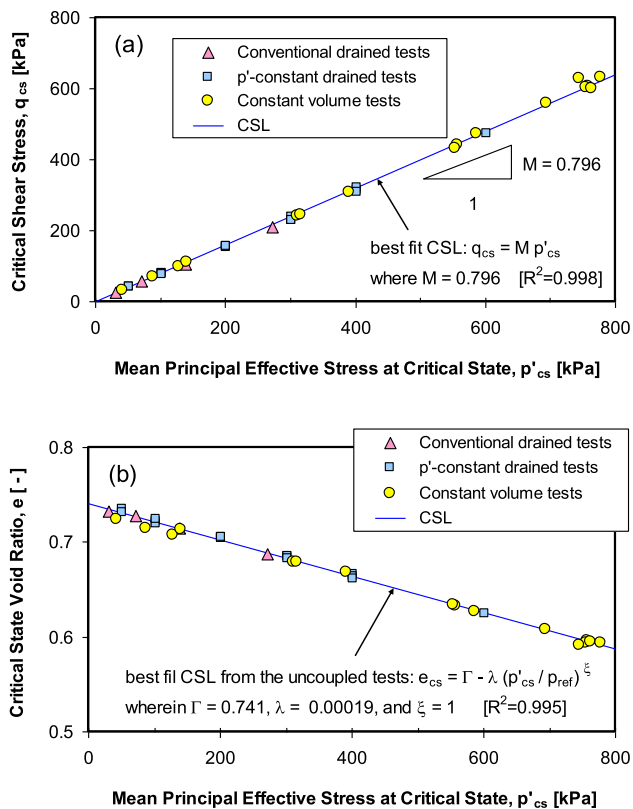


Fig. 4 Simulations for the constant volume TXC behavior of three loose particulate assemblies: **a**  $q$  versus  $\epsilon_q$ ; **b**  $q$  versus  $p'$ ; **c** CN versus  $\epsilon_q$ ; and **d**  $\|dev \mathbf{F}\|$  versus  $\epsilon_q$

$\|dev \mathbf{F}\|_{cs} \approx 0.12$ . The state-dependent variation of the  $\|dev \mathbf{F}\|$  versus  $\epsilon_q$  curves in Figs. 3d and 4d fortify the notion that mobilization of the  $\|dev \mathbf{F}\|$  depends on  $\psi$ .

Li and Wang [36] suggested that the critical state line in granular soils can be expressed through:



**Fig. 5** CSL of the particulate assemblies in the: **a**  $q$  versus  $p'$ ; and **b**  $e$  versus  $p'$  planes

$$q_{cs} = M p'_{cs}; e_{cs} = \Gamma - \lambda \left( \frac{p'_{cs}}{p_{ref}} \right)^\xi \quad (14)$$

wherein  $M$ ,  $\Gamma$ ,  $\lambda$ , and  $\xi$  are the CSL parameters and  $p_{ref} = 101$  [kPa] is a reference stress. To construct the CSL, in addition 34 TXC tests were performed. Using the ultimate states of these TXC tests, the critical state parameters were determined at the end of the simulations (i.e.,  $p'$ ,  $q$ , and  $e$  remained constant upon further shear). The parameters were found to be:  $M = 0.796$  (corresponding to  $\phi'_{cs} = \sin^{-1}[3M/(6+M)] = 20.6^\circ$ ),  $\Gamma = 0.741$ ,  $\lambda = 0.00019$ , and  $\xi \approx 1$ . The CSL of the assemblies in the  $q$  versus  $p'$  and  $e$  versus  $p'$  planes is presented in Fig. 5a, b, respectively.

## 4.2 Strain paths with coupling between the volumetric and axial strains

Figure 6 illustrates the mechanical behaviors of nine initially identical dense ( $e_0 = 0.629$  [-],  $\psi_0 = -0.093$  [-]) particulate assemblies subjected to linear  $\varepsilon_v - \varepsilon_1$  coupling under  $\zeta = -1.0, -0.5, -0.25, -0.1, -0.05, 0, +0.25, +0.5, \text{ and } +1.0$  with  $p'_c = 100$  [kPa]. In fact, the progressive densification/loosening of the assemblies load carrying microstructures caused by the

contractive/expansive volume change results in a full spectrum of behaviors from non-flow strain hardening (see tests under  $\zeta = 0, +0.25, +0.50, \text{ and } +1.0$ ), to post-peak strain softening with flow instability (see tests under  $\zeta = -1.0, -0.50, -0.25, -0.10, \text{ and } -0.05$ ) in Fig. 6a–d. Although the initially identical assemblies were in dense state (since  $\psi_0 = -0.093 < 0$  for all specimens) in the beginning, progressive weakening of load bearing microstructure in the tests with  $\zeta = -0.05$  and  $-0.10$  halted early strain hardening and led to partial loss of the shear strength beyond  $\varepsilon_q = 10$  [%]. Even a forceful flow instability-induced complete loss of shear strength occurred when specimens were imposed to strong expansive linear  $\varepsilon_v - \varepsilon_1$  coupling under  $\zeta = -0.25, -0.50$  and  $-1.0$  [see Fig. 6a–d]. On the contrary, contractive  $\varepsilon_v - \varepsilon_1$  coupling under linear  $\varepsilon_v - \varepsilon_1$  coupling with  $\zeta = +0.25, +0.50$  and  $+1.0$  [see Fig. 6a–d] resulted in continuous strengthening of strain hardening compared to that of the specimen sheared under the constant volume condition (say  $\zeta = 0$ ). Figure 6b, c shows that only state of the specimen sheared under  $\zeta = 0$  condition reached the CSL. Recalling the discussions given in Sect. 3.2, the linear  $\varepsilon_v - \varepsilon_1$  coupling prevents reaching the critical state. Curves drawn in Fig. 7d indicate the strong influence of the linear  $\varepsilon_v - \varepsilon_1$  coupling on the accumulation of the equivalent pore-water pressure calculated from  $\Delta u = \sigma_3 - \sigma'_3$ . In Fig. 6d, complete loss of shear strength (say  $\Delta u = p'_c$ ) due to flow instability happens sooner or later for all specimens sheared under  $\zeta < 0$  depending on the magnitude of  $\zeta$ ; however,  $\Delta u < 0$  was accumulated for the cases with  $\zeta > 0$  following continuous strengthening of load bearing microstructure.

To have a better perspective of the overall strength of the microstructure, curves for CN versus  $\varepsilon_q$  are depicted in Fig. 6e. For the specimen sheared under  $\zeta = 0$ , the gradual drop of CN begins from 5.8 at  $\varepsilon_q = 0$  until CN = 4.9 [-] was reached around  $\varepsilon_q = 4.0$  [%], and thereafter, CN improved steadily to reach 5.3 at the critical state. The complete suppression of shear strength for the specimens sheared under  $\zeta = -0.25, -0.50$  and  $-1.0$  in Fig. 6a agrees with the quick drop of CN from 5.8 to 3.3 [-] in Fig. 6e, and accordingly, the complete loss of internal static stability occurred due to the significant deficiency of active contacts as caused by loosening of the load carrying microstructure.

In the shear strain range studied here, CN in the specimens sheared under  $\zeta = -0.05$  and  $-0.10$  are lower than that under the  $\zeta = 0$  condition; however, a sudden loss of active contacts is expected for these two specimens at larger shear strains. On the other hand, volumetric contraction in the specimens sheared under  $\zeta = +0.25, +0.50$  and  $+1.0$  increased CN



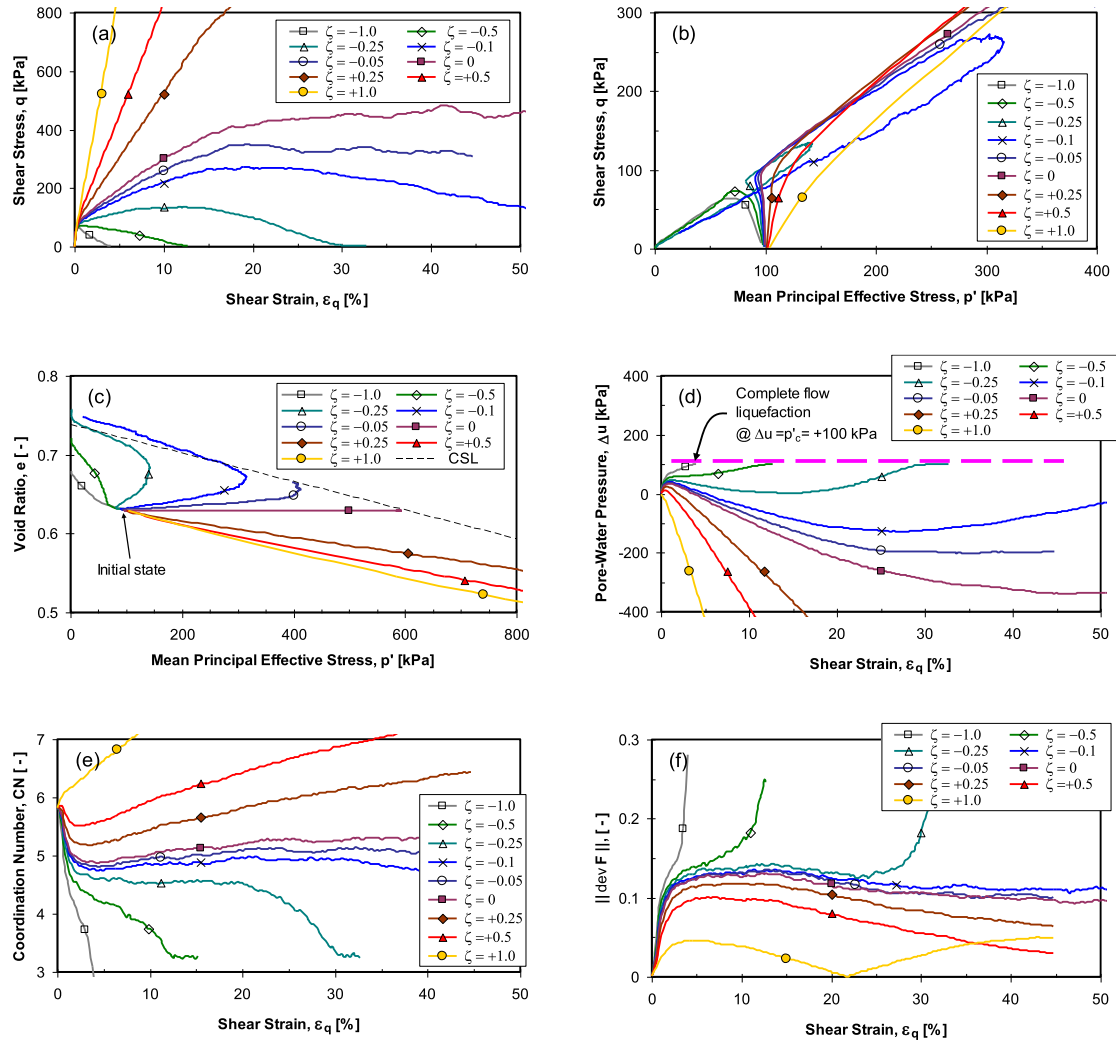


**Fig. 6** Simulations for the influence of linear coupling under  $\zeta = -1.0, -0.5, -0.25, -0.1, -0.05, 0, +0.25, +0.5,$  and  $+1.0$  on the behaviors of nine dense ( $e_0 = 0.629$ ) particulate assemblies with  $p'_c = 100$  [kPa]: **a**  $q$  versus  $\varepsilon_q$ ; **b**  $q$  versus  $p'$ ; **c**  $e$  versus  $\varepsilon_q$ ; **d**  $\Delta u$  versus  $\varepsilon_q$ ; **e** CN versus  $\varepsilon_q$ ; and **f**  $\|\text{dev } \mathbf{F}\|$  versus  $\varepsilon_q$

progressively leading to very stable microstructures as supported by strong strain-hardening responses in Fig. 6a.

The simulated behaviors for eight initially loose ( $e_0 = 0.718$  [-],  $\psi_0 = -0.013$  [-]) particulate assemblies subjected to the linear  $\varepsilon_v$ - $\varepsilon_1$  coupling under  $\zeta = -1.0, -0.50, -0.25, -0.05, 0, +0.10, +0.25$  and  $+0.50$  from  $p'_c = 50$  [kPa] are illustrated in Fig. 7. The loose specimen sheared under  $\zeta = 0$  condition suffered from a long-standing limited flow instability initiating from the onset of the post-peak strain softening around  $\varepsilon_q \approx 1\%$  until  $\varepsilon_q \approx 7\%$  where the specimen strain hardening instigated [see Fig. 7a, b]. Following the progressive loosening of load bearing microstructure associated with expansive volumetric strains [see Fig. 7a-c], all the specimens sheared under  $\zeta < 0$  demonstrated permanent complete loss of shear strength and full accumulation of excess pore-

water pressure (say  $\Delta u = p'_c = 50$  [kPa]) in the post-peak regime of the behavior [see Fig. 7d]. Sudden drop of CN from 4.3 [-] to values less than 3 [-] and simultaneously, quick rises in  $\|\text{dev } \mathbf{F}\|$  in Fig. 7e, f point to complete disintegration of the load bearing microstructure for the specimens sheared with  $\zeta < 0$ . However, in the  $\zeta = 0$  case, CN attained a minimum of 3.2 [-] around  $\varepsilon_q = 3.5\%$  where the specimen lost more than 90 [%] of its peak shear strength, and then, CN improved to  $CN_{cs} \approx 3.4$  [-] upon further shearing. On the other hand, contractive volume changes caused mild to strong non-flow responses and accumulation of negative  $\Delta u$  to occur in the very loose specimens under  $\zeta = +0.10, +0.25$  and  $+0.50$  in Fig. 7a-d.

Conversely, expansive  $\varepsilon_v$ - $\varepsilon_1$  coupling intensified initial decrease in  $p'$ , slowed down mobilization of  $q$  with  $\varepsilon_q$ , and

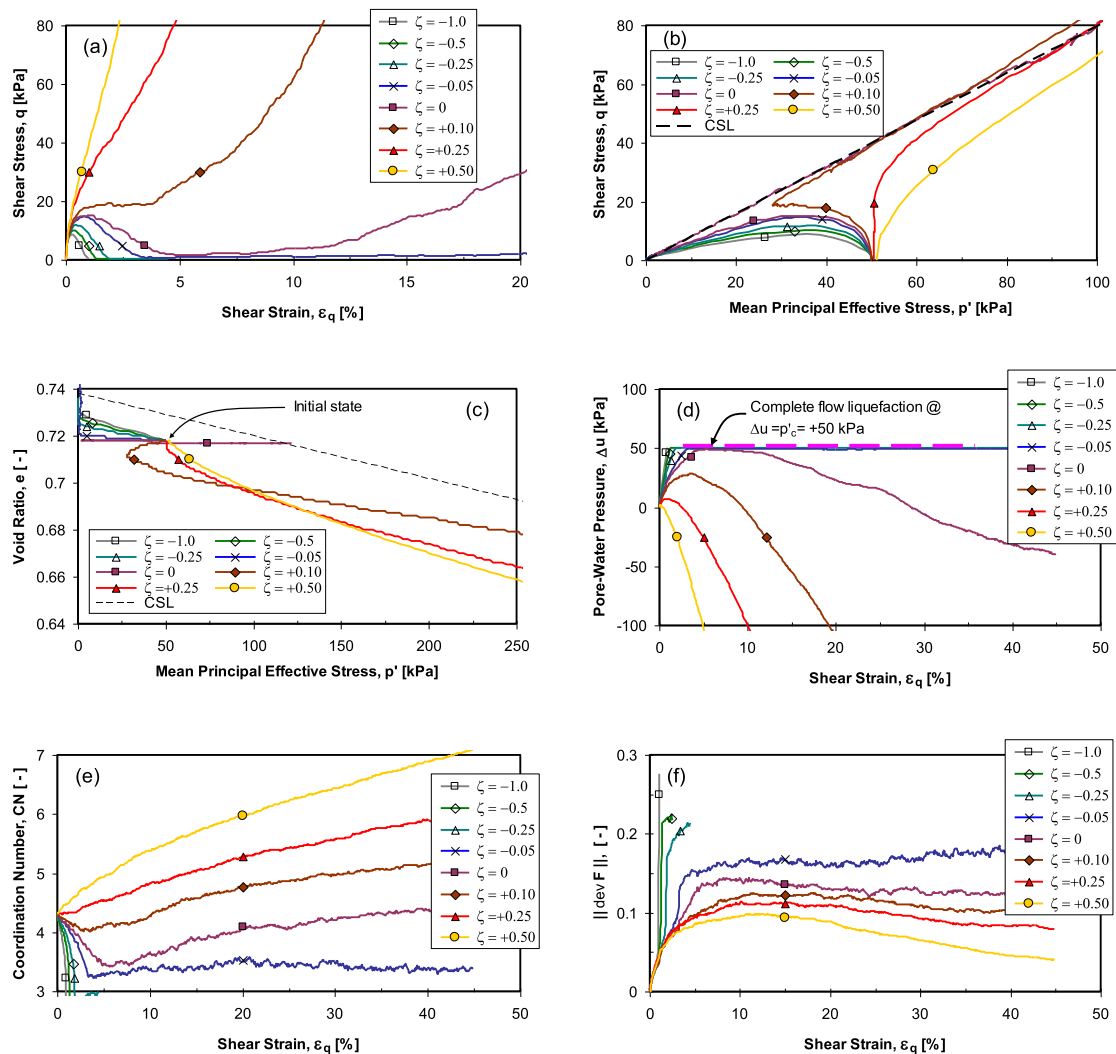


**Fig. 7** Simulations for the influence of linear coupling under  $\zeta = -1.0, -0.5, -0.25, -0.05, 0, +0.10, +0.25,$  and  $+0.5$  on the behaviors of eight loose ( $e_0 = 0.718$ ) particulate assemblies with  $p'_c = 50$  [kPa]: **a**  $q$  versus  $\varepsilon_q$ ; **b**  $q$  versus  $p'$ ; **c**  $e$  versus  $\varepsilon_q$ ; **d**  $\Delta u$  versus  $\varepsilon_q$ ; **e**  $CN$  versus  $\varepsilon_q$ ; and **f**  $\|\text{dev } \mathbf{F}\|$  versus  $\varepsilon_q$

accumulation of  $\Delta u$  with  $\varepsilon_q$ . However, continuous decline in the ultimate shear strength was not the sole outcome of decreasing  $\varepsilon_{v\infty}$  and the specimens with  $\varepsilon_{v\infty} = -1.50$  and  $-2.50$  [%] suffered from post-peak limited flow instability which was intensified significantly by decreasing  $\varepsilon_{v\infty}$ . In Fig. 8c, all  $e$  versus  $p'$  curves ended on the CSL obtained in Fig. 5b. For the assembly sheared under  $\varepsilon_{v\infty} = 0$  in Fig. 8e,  $CN$  suddenly dropped from 5.85 at  $\varepsilon_q \approx 0$  to a minimum of 4.85 [-] around  $\varepsilon_q = 4.75$  [%], and then, it improved asymptotically toward 5.35 [-] as  $\varepsilon_q \rightarrow \infty$ . The initial loss in  $CN$  and peak in  $\|\text{dev } \mathbf{F}\|$  [see Figs. 8e and 9f] decreased with the increase in  $\varepsilon_{v\infty}$  from  $-2.50$  to  $+0.90$  [%]. However, the minimums of  $CN$  were achieved within the range  $\varepsilon_q$  from 2 to 5 [%], while peaks of  $\|\text{dev } \mathbf{F}\|$  were observed around  $\varepsilon_q \approx 10$  [%]. The latter observations may

be attributed to relieve in contact rearrangement under dilative volumetric strains.

Results of similar simulations for initially medium-loose ( $e_0 = 0.706$ ,  $p'_c = 100$  [kPa],  $\psi_0 = -0.025$ ) assemblies subjected to transient  $\varepsilon_v$ - $\varepsilon_1$  coupling with  $\varepsilon_{v\infty} = -0.90, -0.6, -0.30, 0, +0.30, +0.60,$  and  $+0.90$  [%] under  $R = 0.75$  are depicted in Fig. 9. Owing to the increase in  $e_0$ , the specimen sheared under  $\varepsilon_{v\infty} = 0$  showed limited flow response which was followed by a weak strain hardening. Analogous to the previous case, contractive volumetric strains stabilized the mechanical behavior of the assemblies through the increase in the shear strength and decrease in the initial positive  $\Delta u$ . On the other hand, the assemblies sheared under  $\varepsilon_{v\infty} = -0.60$  and  $-0.90$  lost their shear strength almost completely within the shear strain range 5–12 [%]. Also for this case,  $CN$  improved

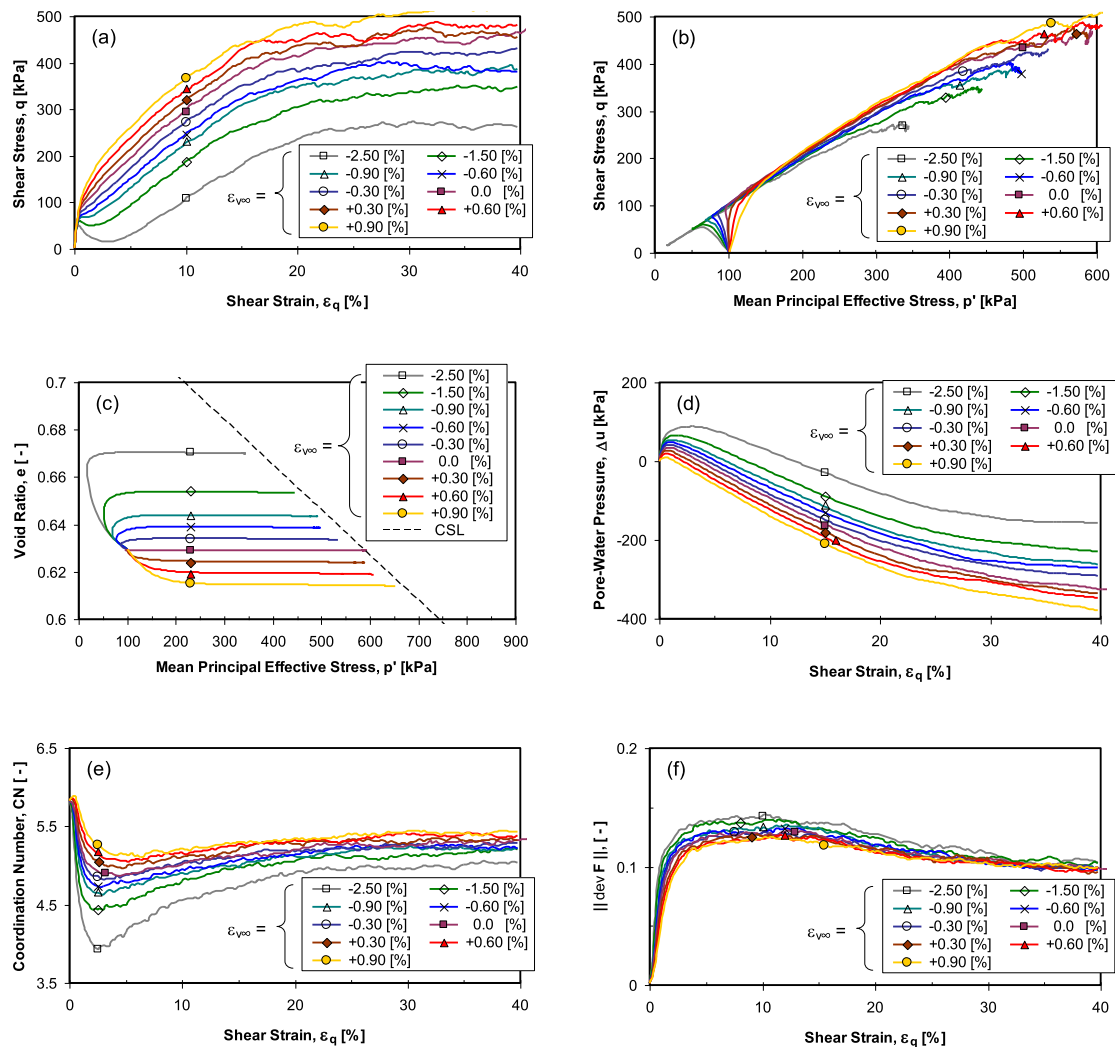


**Fig. 8** Simulations for the influence of exponential coupling under  $R = 0.75$ , and  $\varepsilon_{v\infty} = -2.50, -1.50, -0.90, -0.60, -0.30, 0, +0.30, +0.60$ , and  $+0.90$  [%] on the behaviors of nine dense ( $e_0 = 0.629$ ) particulate assemblies with  $p'_c = 100$  [kPa]: **a**  $q$  versus  $\varepsilon_q$ ; **b**  $q$  versus  $p'$ ; **c**  $e$  versus  $\varepsilon_q$ ; **d**  $\Delta u$  versus  $\varepsilon_q$ ; **e** CN versus  $\varepsilon_q$ ; and **f**  $\|\text{dev } \mathbf{F}\|$  versus  $\varepsilon_q$

slightly with the contractive volumetric strains. On the contrary, CN dropped abruptly for two specimens subjected to dilative volumetric strains with  $\varepsilon_{v\infty} = -0.60$  and  $-0.90$  [-] following loosening of microstructure.

Figure 10 indicates the effect of the initial confining pressure ( $p_0$ ) on the micro- and macroscale responses of soil assemblies, which were sheared with the same initial void ratio of  $e_0 \approx 0.678$  (samples A-13, A-16, and A-28, as outlined in Table 2). In Fig. 10a, representing assemblies under linear coupling, a clear dependency of shear strength on the initial confining pressure is evident for all samples at shear strain levels up to 12 [%]. However, as the strain level increases, all curves converge to a maximum value of shear strength, regardless of the initial confining pressure, and solely dependent on the value of  $\zeta$ . The

ultimate shear strength at higher strain levels ( $\varepsilon_q = 40$  [%]) is primarily influenced by  $\zeta$ . In Fig. 10b, it is evident that all specimens with  $\zeta = 0.05$ , sheared under different initial confining pressures, display a non-flow strain-hardening response. However, reducing  $\zeta$  from 0.05 to  $-0.1$  intensifies the tendency toward a contractive response before reaching the phase transformation state. At  $\zeta = -0.1$ , the effective stress paths do not intersect the phase transformation line at all. Instead, a purely contractive behavior is observed, with the mean effective pressure reaching a zero-stress state at high shear strains. According to Fig. 10c, it is observed that the initial CN is nearly identical for samples with the same  $\zeta$ . However, similarly to the observations made for the shear stress, the value of CN is also influenced by the initial confining pressure at low strain levels (below

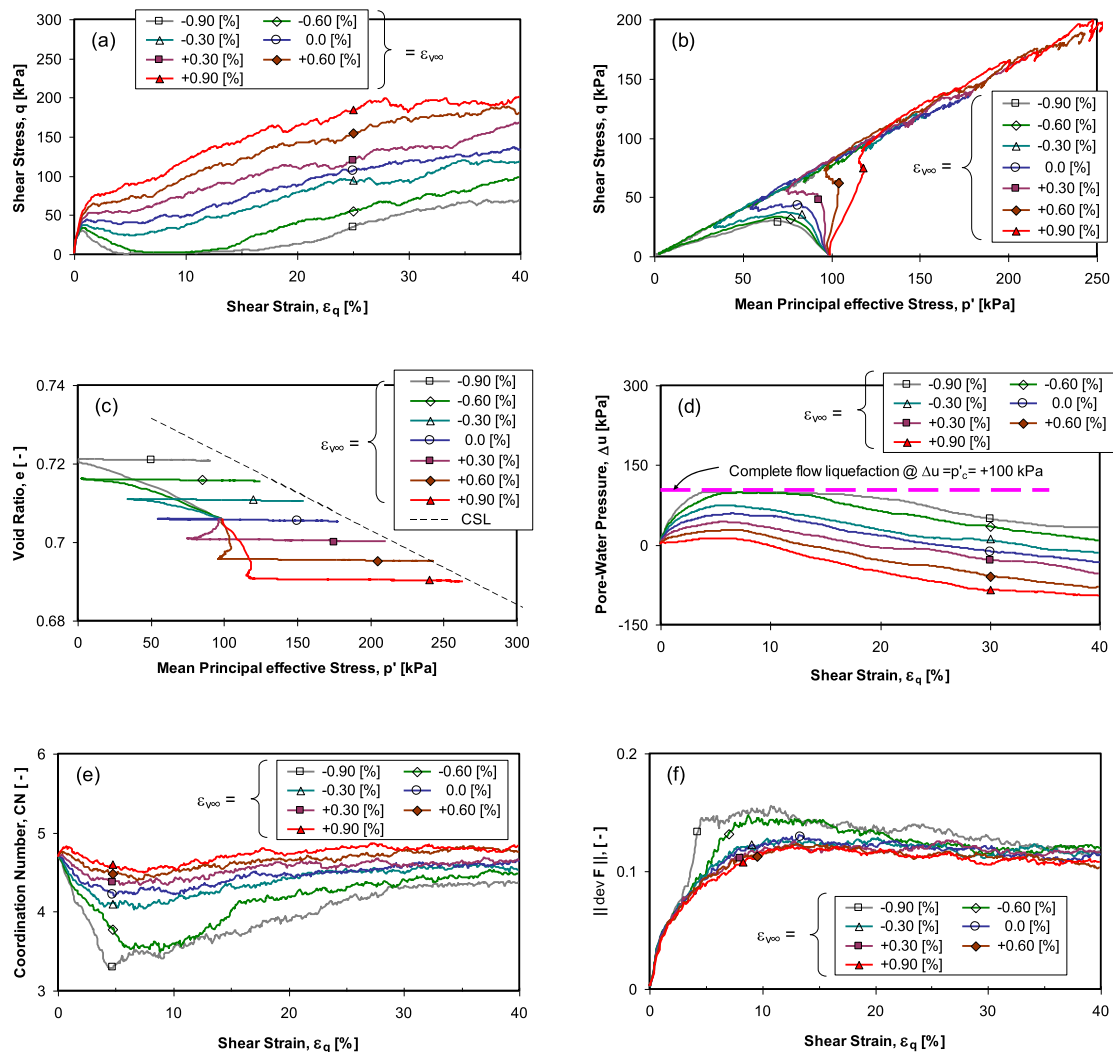


**Fig. 9** Simulations for the influence of exponential coupling under  $R = 0.75$ , and  $\varepsilon_{v\infty} = -0.90, -0.60, -0.30, 0, +0.30, +0.60$ , and  $+0.90$  [%] on the behaviors of seven medium-loose ( $e_0 = 0.706$ ) particulate assemblies with  $p'_c = 100$  [kPa]: **a**  $q$  versus  $\varepsilon_q$ ; **b**  $q$  versus  $p'$ ; **c**  $e$  versus  $\varepsilon_q$ ; **d**  $\Delta u$  versus  $\varepsilon_q$ ; **e** CN versus  $\varepsilon_q$ ; and **f**  $\|\text{dev } \mathbf{F}\|$  versus  $\varepsilon_q$

12 [%]), converging to an ultimate value at higher strain levels. Moreover, as the shear strain increases,  $\zeta$  becomes the determining factor also for the ultimate CN value. Samples with lower  $p_0$  have lower coordination numbers, as shown in Fig. 10c, and higher  $\|\text{dev } \mathbf{F}\|$  values, as depicted in Fig. 10d, at strain levels up to 12 [%]. As the shear strain amplifies, the influence of  $\zeta$  becomes more pronounced and ultimately decides the final value of  $\|\text{dev } \mathbf{F}\|$  as well. Figure 10e–h present simulation results of the behaviors of particulate assemblies under transient coupling paths. A qualitative comparison between Fig. 10e–h and a–d reveals similar effects of  $p_0$  on both macro- and microscale responses. Specifically,  $p_0$  influences the response until a certain strain level, while  $\varepsilon_{v\infty}$  emerges as the primary decisive factor affecting particulate

assemblies' response under high strain levels (beyond  $\varepsilon_q > 20$  [%]).

In Eq. (10),  $R$  controls the pace of change in  $\varepsilon_v$  with  $\varepsilon_1$  and the greater  $R$ , the faster  $\varepsilon_v$  varies to reach  $\varepsilon_{v\infty}$ . The mechanical response of six initially identical medium-loose assemblies ( $e_0 = 0.706$ ,  $p'_c = 100$  [kPa], and  $\psi_0 = -0.025$ ) under  $R = 0.75, 0.45, 0.35, 0.25, 0.15$ , and  $0.05$  with  $\varepsilon_{v\infty} = -0.60$  [%] are simulated in Fig. 11. The transient  $\varepsilon_v$ – $\varepsilon_1$  coupling paths and the corresponding  $e$  versus  $p'$ ,  $q$  versus  $\varepsilon_q$ ,  $q$  versus  $p'$  responses are, respectively, depicted in Fig. 11a–d. Even though the target asymptotic void ratio was slightly (change in void ratio is  $\Delta e = -(1 + e_0) \varepsilon_{v\infty} \approx +0.0102$ ) greater than  $e_0$  [see Fig. 11b], Fig. 11c, d indicates that  $R$  played a profound role in the overall macroscale response of the assemblies in

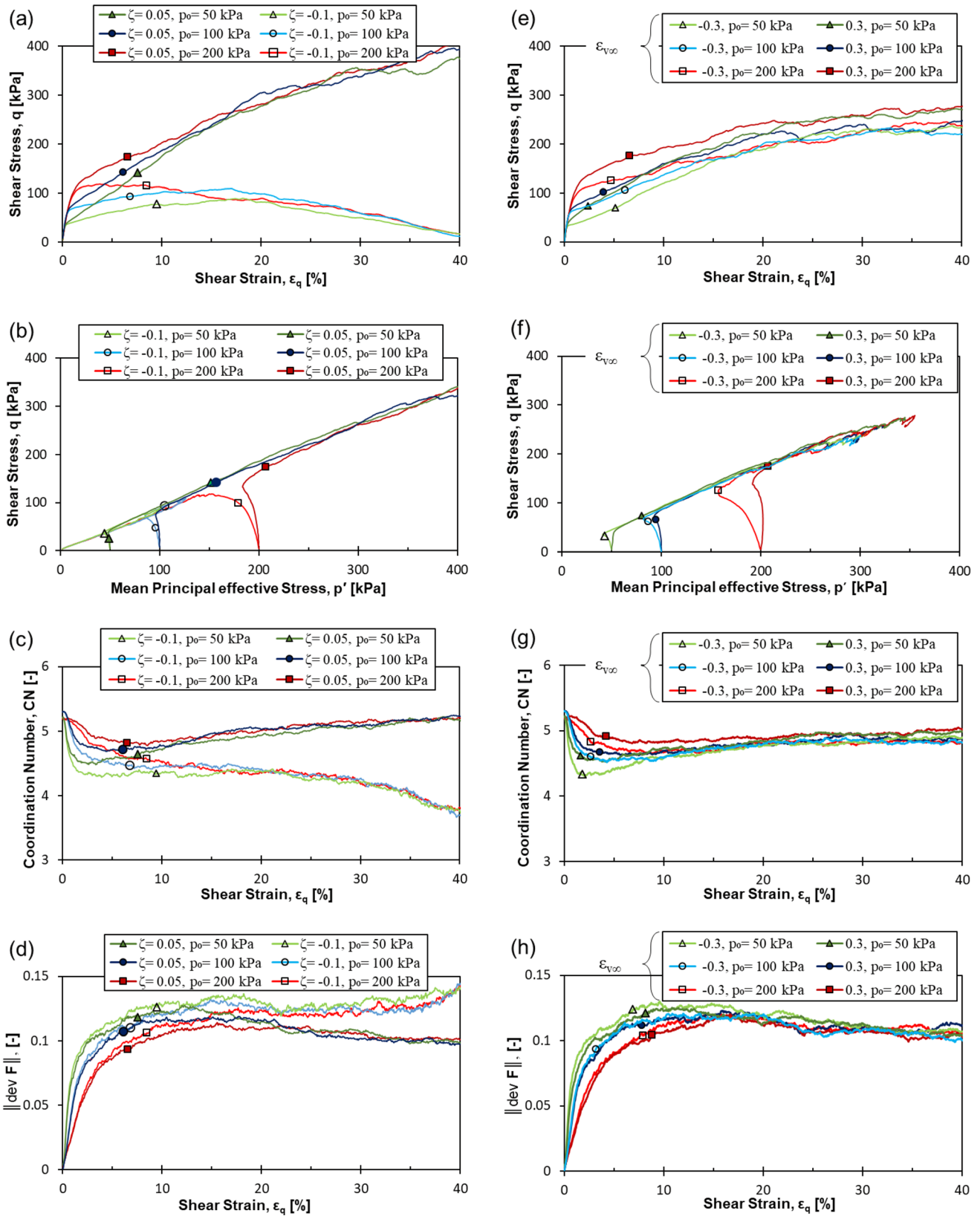


**Fig. 10** Simulations for the influence of initial mean stress on the behaviors of three medium-loose particulate assemblies under linear (left side) and exponential (right side) coupling with the same initial void ratio ( $e_0 \approx 0.678$ ) under  $p_c = 50, 100,$  and  $200$  [kPa]: **a** and **e**  $q$  versus  $\epsilon_q$ ; **b** and **f**  $q$  versus  $p'$ ; **c** and **g**  $CN$  versus  $\epsilon_q$ ; **d** and **h**  $\|dev F\|$  versus  $\epsilon_q$



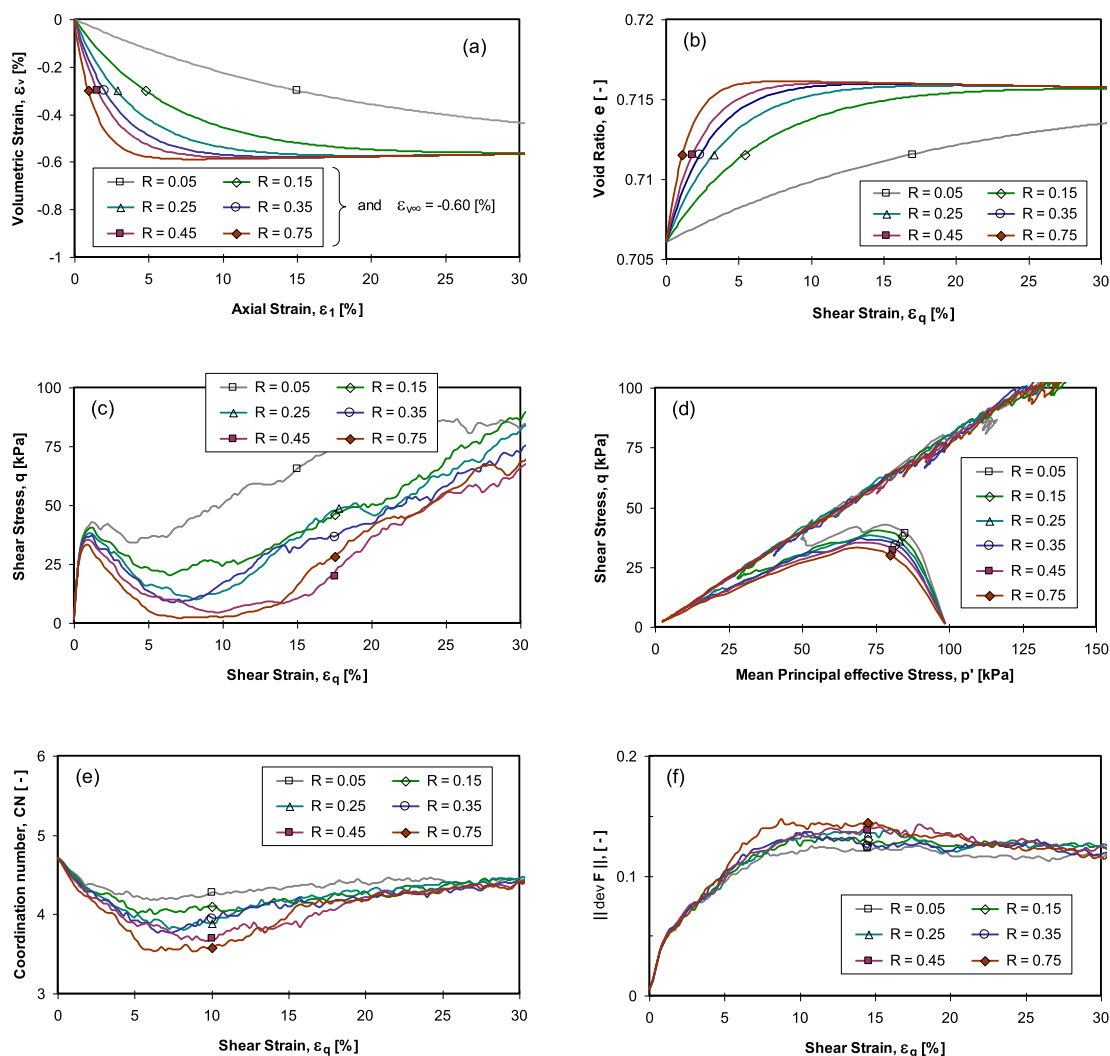


**Fig. 11** Simulations for the influence of exponential dilatant transient coupling under  $\varepsilon_{v\infty} = -0.60$  [%] and  $R = 0.75, 0.45, 0.35, 0.25, 0.15$ , and  $0.05$  on the behaviors of seven medium-loose ( $e_0 = 0.706$ ) particulate assemblies with  $p'_c = 100$  [kPa]: **a**  $\varepsilon_v$  versus  $\varepsilon_1$ ; **b**  $e$  versus  $\varepsilon_q$ ; **c**  $q$  versus  $\varepsilon_q$ ; **d**  $q$  versus  $p'$ ; **e** CN versus  $\varepsilon_q$ ; and **f**  $\|\text{dev } \mathbf{F}\|$  versus  $\varepsilon_q$

as much as its increase intensified post-peak softening remarkably.

However, a unique ultimate shear strength is expected to reach by all specimens at large shear strains owing to gradual nullification of  $\varepsilon_v$ - $\varepsilon_1$  coupling at identical target void ratio [say  $e_0 - (1 + e_0)\varepsilon_{v\infty}$ ]. Figure 11e, f signify that the transient minimums in CN decrease with  $R$ , while the peak  $\|\text{dev } \mathbf{F}\|$  values increased with  $R$ . Nonetheless, the asymptotic CN and  $\|\text{dev } \mathbf{F}\|$  values are practically identical irrespective of  $R$ . Similar numerical simulations for three initially identical assemblies ( $e_0 = 0.706$  [-],  $p'_c = 100$  [kPa], and  $\psi_0 = -0.025$  [-]) sheared under  $R = 0.75, 0.45$ , and  $0.15$  with contractive  $\varepsilon_{v\infty} = +0.60$  [%] are depicted in Fig. 12 [see Fig. 12a, b for the strain paths and  $e$  vs.  $\varepsilon_q$  curves]. A side-by-side comparison of parts “c” to “f” of

Fig. 12 with the corresponding ones in Fig. 11 indicates that change in  $R$  under contractive  $\varepsilon_v$ , at least for the range of values studied here, does not change  $q$  versus  $\varepsilon_q$ ,  $q$  versus  $p'$ , CN versus  $\varepsilon_q$ , and  $\|\text{dev } \mathbf{F}\|$  versus  $\varepsilon_q$  responses, profoundly.

Soon after a seismic event, pore-water pressure redistribution may occur following migration of pore water from high-pressure regions to the low-pressure ones. Figure 6, 7, 8, and 9 imply that pore-water influx-induced expansion of soil elements (as caused by  $\zeta > 0$  and  $\varepsilon_{v\infty} > 0$ ) weakens sand strength against flow liquefaction instability significantly. Moreover, the increase in rate of pore-water influx intensifies post-peak softening after triggering of flow liquefaction instability. In contrast, pore-water outflux causes volumetric contraction and mitigates

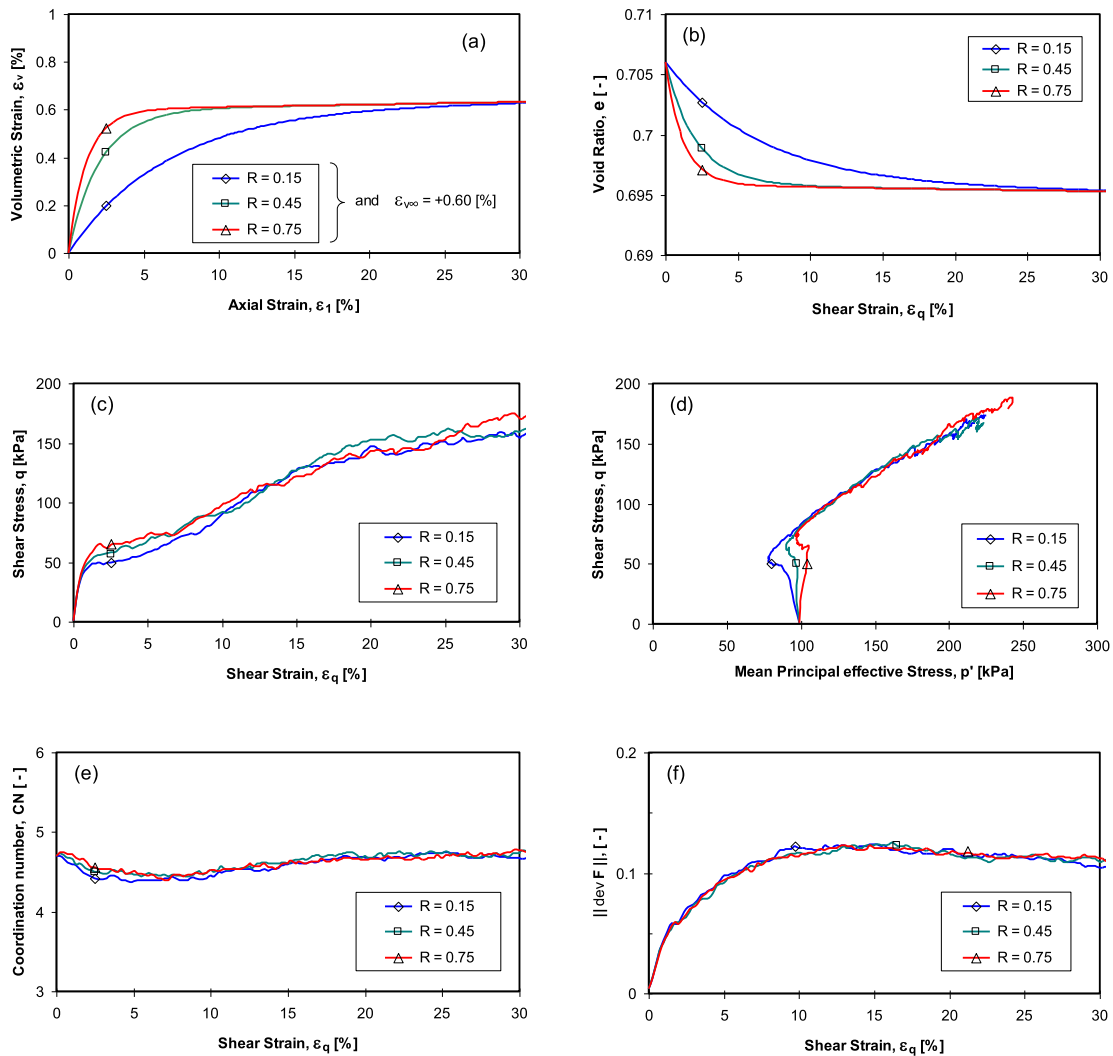


**Fig. 12** Simulations for the influence of exponential contractive transient coupling under  $\varepsilon_{v0} = +0.60$  [%] and  $R = 0.75, 0.45,$  and  $0.15$  on the behaviors of three medium-loose ( $e_0 = 0.706$ ) particulate assemblies with  $p'_c = 100$  [kPa]: **a**  $\varepsilon_v$  versus  $\varepsilon_1$ ; **b**  $e$  versus  $\varepsilon_q$ ; **c**  $q$  versus  $\varepsilon_q$ ; **d**  $q$  versus  $p'$ ; **e**  $CN$  versus  $\varepsilon_q$ ; and **f**  $\|dev F\|$  versus  $\varepsilon_q$

flow liquefaction vulnerability depending on the amount and rate of pore-water outflux.

### 4.3 Critical state of specimens sheared under transient $\varepsilon_v$ - $\varepsilon_1$ coupling

A condition of nil volume change while soil element continues shearing without any further change in effective stress tensor is a prerequisite for the critical state (e.g., [5, 13, 20, 47, 70]). Nullification of  $\varepsilon_v$  never fulfills in strain paths with linear  $\varepsilon_v$ - $\varepsilon_1$  coupling, and accordingly, such strain paths are unable to direct soil state toward the CSL [see Sect. 3.2]. However,  $\varepsilon_v$  is gradually terminated in strain paths with transient  $\varepsilon_v$ - $\varepsilon_1$  coupling. The ultimate states of specimens sheared under  $\varepsilon_{v0} = -2.50, -1.50,$

$-0.90, -0.60, -0.30, +0.30, +0.60,$  and  $+0.90$  [%] are depicted in the  $q$  versus  $p'$  [see Fig. 13a] and  $e$  versus  $p'$  [see Fig. 13b] planes. For the sake of comparison, the critical state data achieved from uncoupled tests [i.e., constant volume, conventional drained and  $p'$ -constant drained tests in Sect. 4.1] are also superimposed on the figures. Figure 13a, b indicates that a single CSL describes the ultimate states of the assemblies sheared under uncoupled stress paths and the ones sheared with transient  $\varepsilon_v$ - $\varepsilon_1$  coupling.

Similarly, the data for  $CN_{cs}$  versus  $p'_{cs}$ ,  $\|dev F\|_{cs}$  versus  $CN_{cs}$  and  $\|dev F\|_{cs}$  versus  $p'_{cs}$ , respectively, illustrated in Fig. 13c-e are uniquely interrelated with each other in the numerical simulations of the uncoupled stress paths as well as strain paths with transient  $\varepsilon_v$ - $\varepsilon_1$  coupling. Using the data

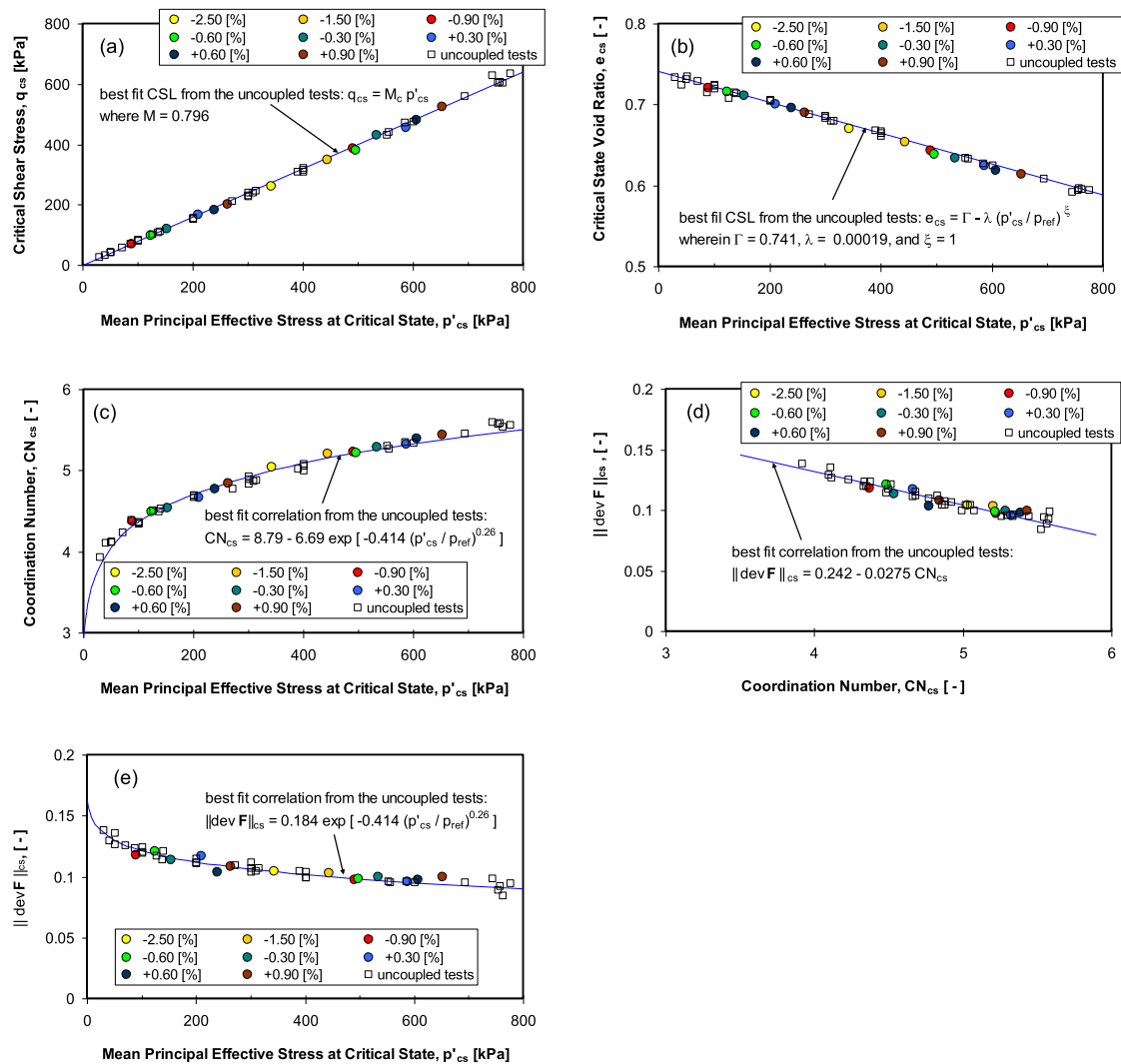


**Fig. 13** Critical state characteristics of the assemblies subjected to transient coupling between the volumetric and axial strains: **a** CSL in the  $q$  versus  $p'$  plane; **b** CSL in the  $e$  versus  $p'$  plane; **c**  $CN_{cs}$  versus  $p'_{cs}$ ; **d**  $\|dev \mathbf{F}\|_{cs}$  versus  $CN_{cs}$ ; and **e**  $\|dev \mathbf{F}\|_{cs}$  versus  $p'_{cs}$

of  $CN_{cs}$  for a total of 34 uncoupled tests in Fig. 13c leads to the following nonlinear empirical correlation between  $CN_{cs}$  and  $p'_{cs}$ :

$$CN_{cs} = 8.79 - 6.69 \exp \left[ -0.414 \left( \frac{p'_{cs}}{p_{ref}} \right)^{0.26} \right] \quad (15)$$

It is observed that Eq. (15) can reasonably predict the  $CN_{cs}$  versus  $p'_{cs}$  data for the uncoupled and transient coupling tests in Fig. 13c. The data in Fig. 13d suggest a linear correlation between  $\|dev \mathbf{F}\|_{cs}$  and  $CN_{cs}$ :

$$\|dev \mathbf{F}\|_{cs} = 0.242 - 0.0275 CN_{cs} \quad (16)$$

Equations (15) and (16) imply that an increase in  $p'_{cs}$  [or a decrease in  $e_{cs}$  from Eq. (14)<sub>b</sub>] results in an increase in  $CN_{cs}$  and subsequently a decrease in  $\|dev \mathbf{F}\|_{cs}$ . Figure 13e

corroborates that  $\|dev \mathbf{F}\|_{cs}$  versus  $p'_{cs}$  data vary in a narrow range in a way that the increase in  $p'_{cs}$  causes a decrease in  $\|dev \mathbf{F}\|_{cs}$  that can be expressed through the following empirical relationship:

$$\|dev \mathbf{F}\|_{cs} = 0.184 \exp \left[ -0.414 \left( \frac{p'_{cs}}{p_{ref}} \right)^{0.26} \right] \quad (17)$$

## 5 Anisotropy of contact force networks

Inter-particle contact forces in granular systems are transmitted by means of contact force networks. Azéma and Radjai [4], Guo and Zhao [14], Zhou et al. [71], Shi and Guo [55], and Liu et al. [37] have addressed the bimodal

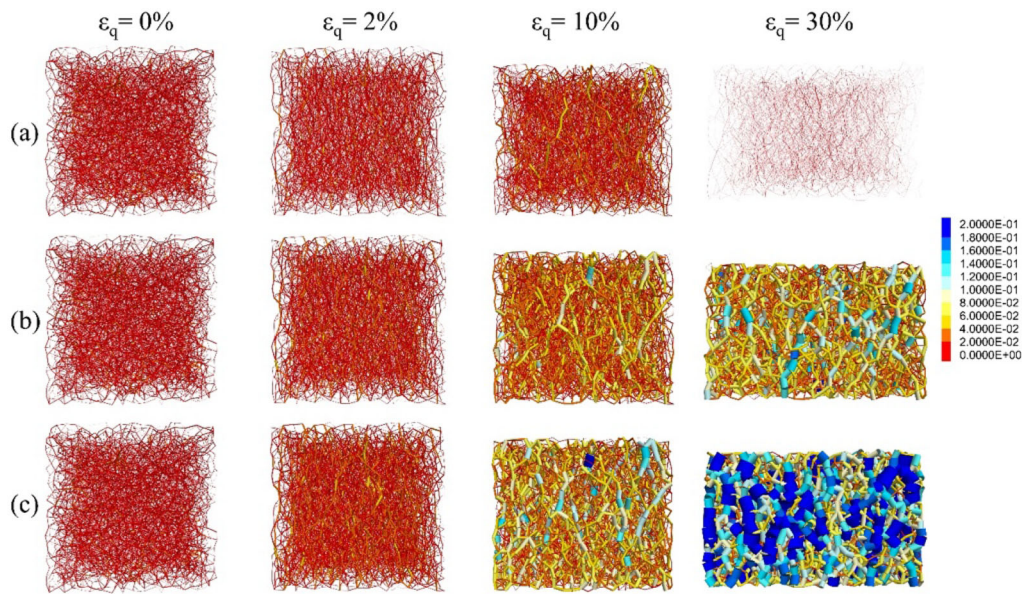


**Fig. 14** Evolution of strong force network with shear strain in tests with the linear coupling between the volumetric and shear strains on three specimens with  $e_0 = 0.629$  and  $p'_c = 100$  [kPa]: **a**  $\zeta = -0.25$ , **b**  $\zeta = 0$ , and **c**  $\zeta = +0.25$

nature of the force network and partitioned it into the strong and weak networks. In the strong network, the transmitted forces are greater than a certain threshold and distribution of force chains may demonstrate a considerable anisotropy leading to anisotropic macroscale response of the assembly. On the other hand, contact forces less than the threshold value form the weak network and their spatial distribution remains almost unchanged during loading. Inspired by Azéma and Radjai [4], Guo and Zhao [14], and Shi and Guo [55] among others,  $f_{thr} = \langle f \rangle$  is adopted here as the dividing threshold whereby  $\langle f \rangle$  is the average value of the transmitted forces in the force network.

To understand the macro-mechanical behavior of assemblies when subjected to linear coupling, three dense assemblies were studied. These assemblies were subjected to linear  $\varepsilon_v - \varepsilon_1$  coupling with  $\zeta$  values of  $-0.25$ ,  $0.0$ , and  $+0.25$  as shown in Fig. 6. The evolution of the strong force networks at  $\varepsilon_q$  values of  $0$ ,  $2$ ,  $10$ , and  $30$  [%] is shown in Fig. 14a–c. After isotropic compression and prior to shear, the average contact force in strong network of the identical specimens was uniformly distributed and amounted  $0.00757$  [N], which corresponds to an initial isotropic stress condition. For the three specimens, a slight increase in the strong force networks is observed at  $\varepsilon_q = 2$  [%] which may be attributed to the increase in shear stress at the early stage of shearing [see Fig. 6a]. However, at this stage, the distribution of the strong network force remains generally isotropic. In Fig. 14a, loosening of the strong force networks emerges for higher shear strains until the end of the experiment with  $\zeta = -0.25$  in a way that the average force magnitudes in the strong networks amounted

$0.0110$ ,  $0.0173$ , and  $0.00006$  [N] corresponding to  $\varepsilon_q = 2$ ,  $10$ , and  $30$  [%], respectively. Clearly, up to  $\varepsilon_q = 10$  [%], the shear stress shown in Fig. 6a for  $\zeta = -0.25$  increases, which results from the increase in contact forces as illustrated in Fig. 14a. Furthermore, as the shear stress increases, the vertical stress  $\sigma_1$  also increases, a result of the development of anisotropic contact forces, particularly in the vertical direction at this strain level [see Fig. 14a]. Finally, at high strains, the shear stress decreases, which is attributed to the diminishing contact force network. For the assembly sheared under the constant volume condition [see Fig. 14b], the strong force networks improve gently and the average force magnitudes of  $0.0139$ ,  $0.03458$ , and  $0.05949$  [N] were obtained at  $\varepsilon_q = 2$ ,  $10$ , and  $30$  [%], respectively. For the assembly sheared under contractive  $\varepsilon_v - \varepsilon_1$  coupling with  $\zeta = +0.25$  [see Fig. 14c], the strong networks fortified progressively in view of the fact that the average force magnitudes of  $0.01718$ ,  $0.05230$ , and  $0.1147$  [N] were obtained at  $\varepsilon_q = 2$ ,  $10$ , and  $30$  [%], respectively. The increase in strong force networks, along with the progressive alignment of strong contact forces in the vertical direction, leads to an increase in vertical stress and consequently a progress in the shear stress as shown in Fig. 6a for  $\zeta = 0.0$ , and especially for  $\zeta = -0.25$ .

For three medium-loose assemblies sheared under transient  $\varepsilon_v - \varepsilon_1$  coupling with  $\varepsilon_{v\infty} = -0.90$ ,  $0.0$ , and  $+0.90$  [%] in Fig. 9, evolution of strong force networks is demonstrated in Fig. 15. The average contact force in the strong networks of identical assemblies was  $0.01175$  [N] just prior to shear. At this stage, due to isotropic stress conditions, the contact forces are also distributed



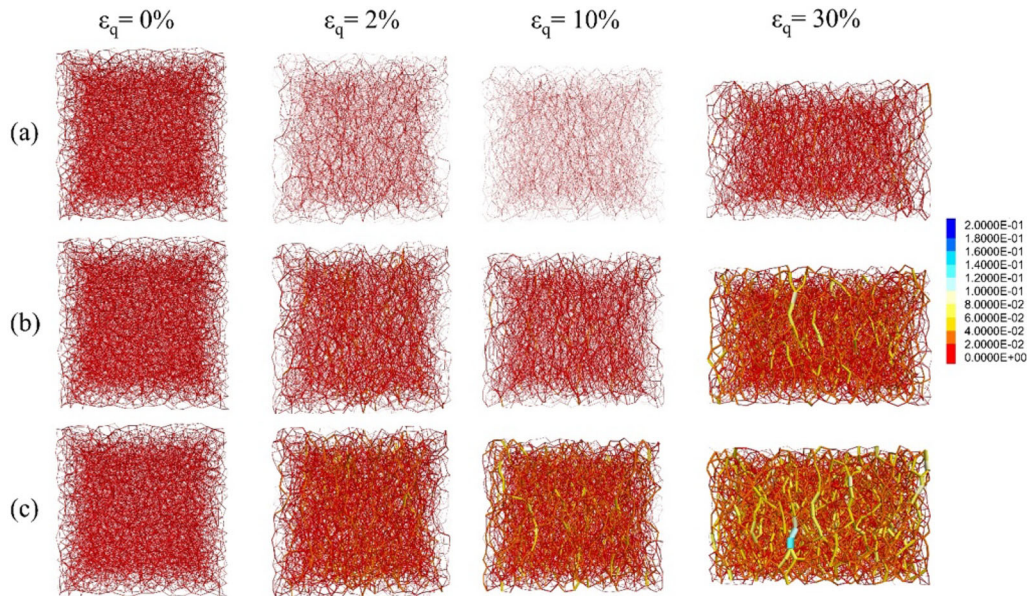


**Fig. 15** Evolution of strong force network with shear strain in tests with transient coupling between the volumetric and shear strains on three specimens with  $e_0 = 0.706$  and  $p'_c = 100$  [kPa]: **a**  $\varepsilon_{v\infty} = -0.9$  [%], **b**  $\varepsilon_{v\infty} = 0$ , and **c**  $\varepsilon_{v\infty} = +0.9$  [%]

isotropically. It is important to note that the higher value of the void ratio accounts for the higher average contact force in the strong networks under the same confining pressure (lower value of coordination number). For the assembly sheared under  $\varepsilon_{v\infty} = -0.90$  [%], the average contact force in the strong networks dropped steadily to reach a minimum of 0.00034 [N] around  $\varepsilon_q = 10$  [%], and then, it improved increasingly and reached 0.00966 [N] at  $\varepsilon_q = 30$  [%], which is reflected in the development of the shear stress in Fig. 9a. A similar trend is observed in the build-up of excess or negative pore-water pressure, resulting from the decrease or increase in the mean effective pressure, respectively, as depicted in the  $e$  versus  $p'$  space in Fig. 9c. Since the variation of shear stress compared to the mean effective stress is not significant, a nearly isotropic distribution of the strong force network is observed in Fig. 15a during almost all stages.

In the specimen sheared under nil volume change ( $\varepsilon_{v\infty} = 0$ ), the average contact force in the strong networks decreased slightly to a minimum of 0.0090 [N] around  $\varepsilon_q = 10$  [%], and thereafter, it increased until the average contact force of 0.01981 [N] was achieved at  $\varepsilon_q = 30$  [%]. The assembly sheared under  $\varepsilon_{v\infty} = +0.90$  shows no transient weakening of the strong force networks, and the average contact force increase until 0.03039 [N] was reached at  $q = 30$  [%]. These observations align with the macro-mechanical illustrations in Fig. 9a, c, where a decrease in the strong force network correlates with a decrease in mean effective stress and shear stress, while an increase in the strong force network leads to an increase in mean effective stress at a constant or decreasing void ratio.

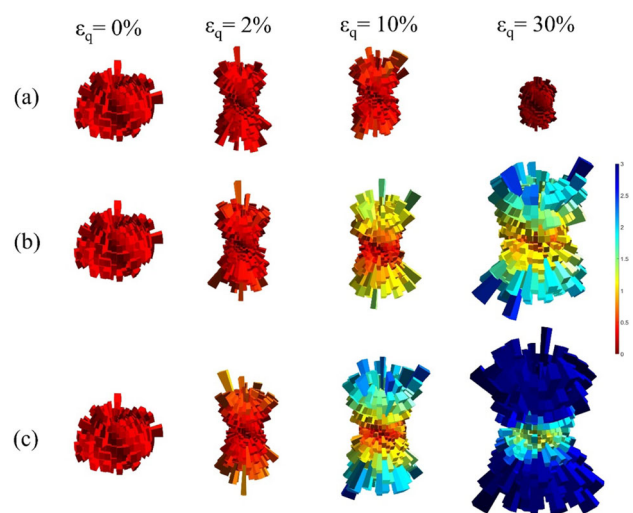


**Fig. 16** 3D histograms for evolution of contact fabric with shear strain in tests with the linear  $\varepsilon_v$ - $\varepsilon_1$  coupling with  $e_0 = 0.629$  and  $p'_c = 100$  [kPa] under: **a**  $\zeta = -0.25$ , **b**  $\zeta = 0$ , and **c**  $\zeta = +0.25$

Furthermore, the development of anisotropy in the direction of the strong force network, coupled with the simultaneous growth of the strong force network, results in an increase in shear stress.

The random distribution of strong force networks in Figs. 14 and 15 at  $\varepsilon_q = 0$  highlights nearly initial isotropy of the load carrying microstructure prior to the shear. However, horizontal force chains were gradually diminished and a majority of the force chains were aligned vertically (parallel with the major principal stress axis) with increasing  $\varepsilon_q$  visualizing gradual formation of strong



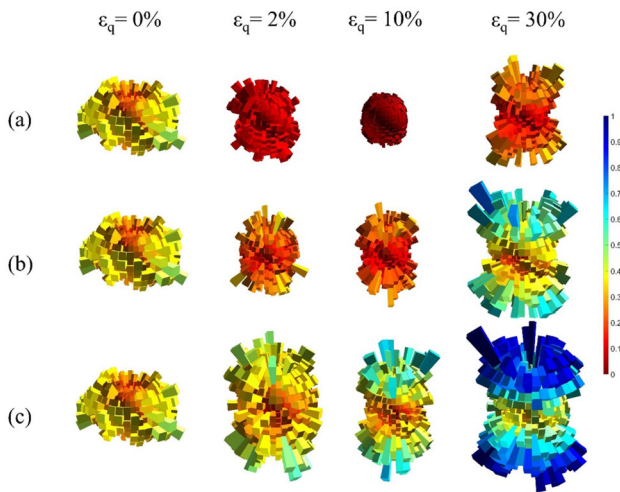


**Fig. 17** 3D histograms for evolution of contact fabric with shear strain in tests with transient  $\varepsilon_v\text{-}\varepsilon_l$  coupling with  $e_0 = 0.706$  and  $p'_c = 100$  [kPa] under: **a**  $\varepsilon_{v\infty} = -0.9$  [%], **b**  $\varepsilon_{v\infty} = 0$ , and **c**  $\varepsilon_{v\infty} = +0.9$  [%]

contact anisotropy in the assemblies. It is worth noting that assemblies undergoing contractive coupled paths, both linear and transient coupling, exhibit evident force chain pathways through particles, which facilitate the transmission of contact forces significantly larger than the average. Conversely, under expansive coupled paths, a discernible shift occurs in the pattern of load transfer within the

assemblies. In such cases, grain loops or clusters surrounding the force chains form what is referred to as the weak force chain, playing a crucial role in stabilizing these linear patterns.

3D histograms of the contact force networks for three dense specimens subjected to linear coupling with  $\zeta = -0.25, 0$ , and  $+0.25$  (see Fig. 6) at  $\varepsilon_q = 0, 2, 10$ , and  $30$  [%] are illustrated in Fig. 16a–c. At  $\varepsilon_q = 0$ , the specimens are nearly isotropic with almost no preferential orientation of contact forces. For the dilative linear coupling with  $\zeta = -0.25$  [see Fig. 16a], the contact force networks became highly anisotropic at  $\varepsilon_q = 2$  [%] and thereafter became shrunk and more isotropic steadily with further straining. On the other hand, for the constant volume case with  $\zeta = 0$  as well as contractive linear coupling with  $\zeta = +0.25$ , applying shear strain caused continuous strengthening of the contact force networks and made their distribution progressively anisotropic until the end of simulation in Figs. 16b, c. 3D histograms of the contact force networks for three medium-loose assemblies sheared under transient coupling with  $\varepsilon_{v\infty} = -0.90, 0$ , and  $+0.90$  (see Fig. 11) computed at  $\varepsilon_q = 0, 2, 10$ , and  $30$  [%] are demonstrated in Fig. 17a–c. For the case with transient  $\varepsilon_v\text{-}\varepsilon_l$  coupling under  $\varepsilon_{v\infty} = -0.90$  [see Fig. 16a], 3D histograms got smaller steadily until  $\varepsilon_q = 10$  [%] was reached, and then, the assembly became progressively anisotropic with further straining. However, for the constant volume

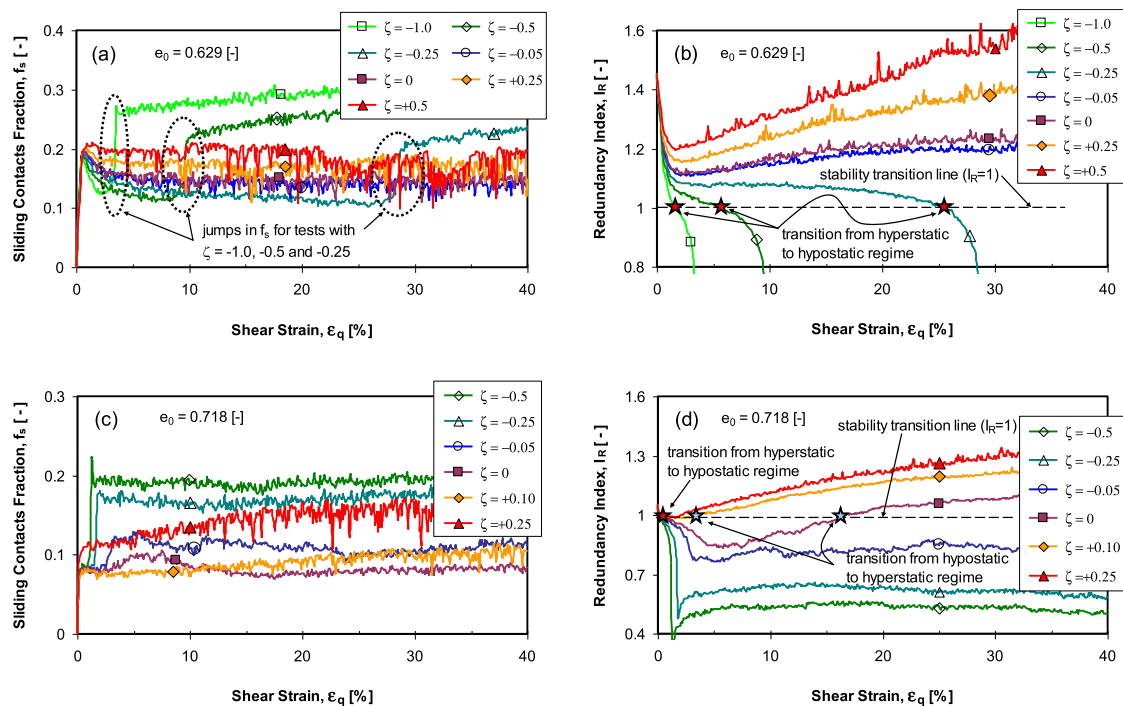


**Fig. 18** Sliding contacts fraction, and redundancy index for: **a** and **b** seven dense ( $e_0 = 0.629$ ) particulate assemblies under linear coupling with  $\zeta = -1.0, -0.50, -0.25, -0.05, 0, +0.25$ , and  $+0.50$ ; **c** and **d** six loose ( $e_0 = 0.718$ ) particulate assemblies under linear coupling with  $\zeta = -0.50, -0.25, -0.05, 0, +0.10$ , and  $+0.25$  [%] sheared from  $p'_c = 100$  [kPa]

(say  $\varepsilon_{v\infty} = 0$ ) and contractive transient  $\varepsilon_v - \varepsilon_1$  coupling under  $\varepsilon_{v\infty} = -0.90$ , 3D histograms of the contact forces became increasingly anisotropic in Fig. 17b, c.

## 6 Investigation of instability

### 6.1 Redundancy index

In Fig. 18a, the sliding contact fraction  $f_s$  [see Sect. 2.1 for the definitions of  $f_s$  and  $I_R$ ] of the dense specimens sheared under linear  $\varepsilon_v - \varepsilon_1$  coupling with  $\zeta = -1.0, -0.50$ , and  $-0.25$  [see Fig. 6 for the tests] is almost doubled following abrupt jumps at  $\varepsilon_q \approx 3.4, 9.7$ , and  $28.3$  [%], respectively, and thereafter, the redundancy index  $I_R$  drops

below 1.0 and the specimens become hypostatic [as marked by red asterisks in Fig. 18b]. The latter observation and sudden decrease in CN in Fig. 6e are definite signs of flow instability in the aforementioned tests. For the tests sheared under linear  $\varepsilon_v - \varepsilon_1$  coupling with  $\zeta = 0.0, +0.25$ , and  $+0.50$ ,  $I_R$  initially drops from 1.45 to 1.12, 1.16, and 1.21, respectively, which are all sufficiently greater than 1. Subsequently,  $I_R$  increases steadily with  $\varepsilon_q$ . Therefore, the assemblies sheared under  $\zeta = 0.0, +0.25$ , and  $+0.50$  always remain hyperstatic and resistant to flow instability. For the loose assemblies in Fig. 18c [see Fig. 7 for the tests], the abrupt jumps in the  $f_s$  versus  $\varepsilon_q$  curves diminish gradually with increasing  $\zeta$  in so far as no jump is observed for the tests with  $\zeta = +0.10$  and  $+0.25$ . At  $\varepsilon_q = 0$  in Fig. 7e, CN is slightly above 4.0 for identical loose

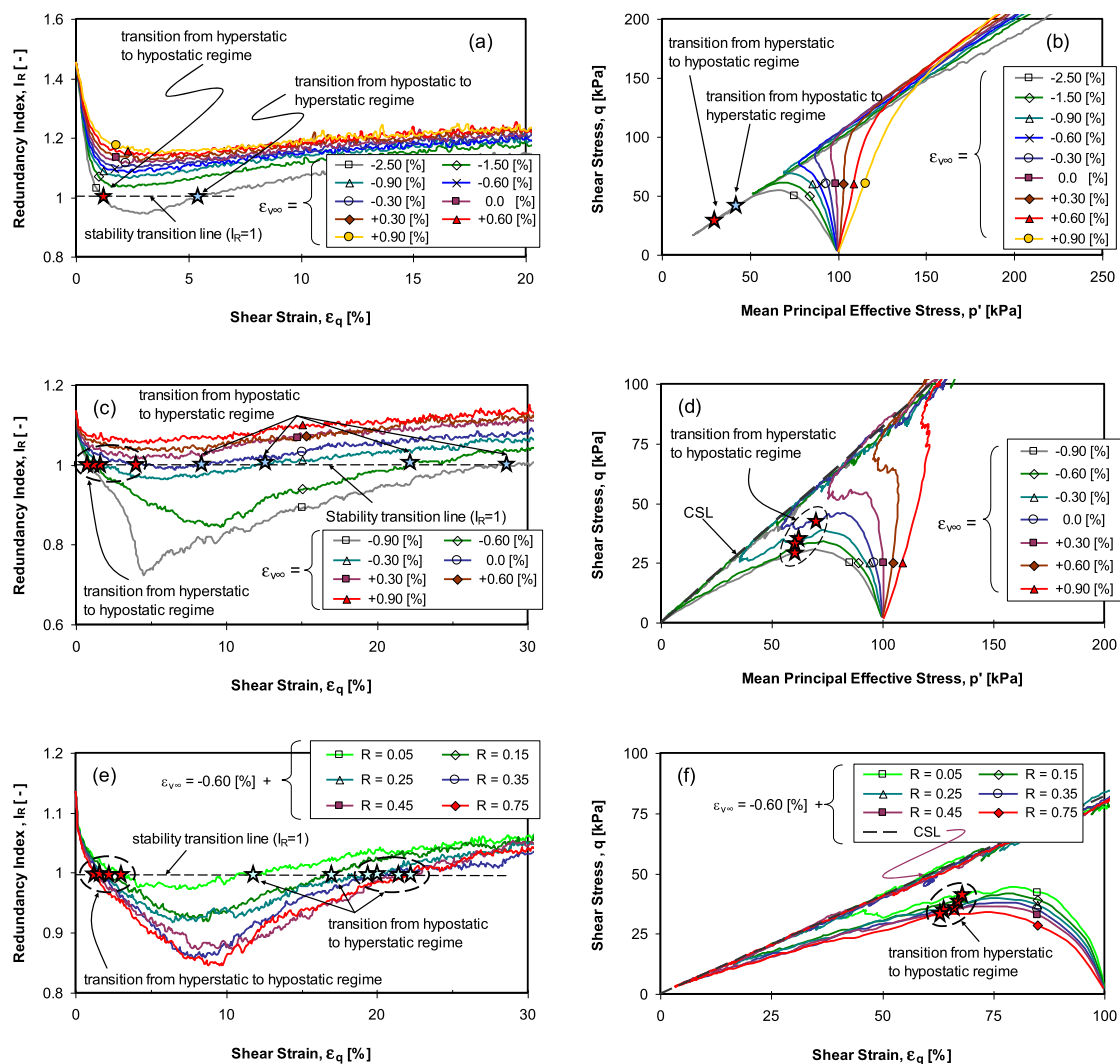


**Fig. 19** Redundancy index and onset of the mechanical instability for: **a** and **b** nine dense ( $e_0 = 0.629$ ) assemblies under  $R = 0.75$  and  $\varepsilon_{v\infty} = -2.50, -1.50, -0.90, -0.60, -0.30, 0, +0.30, +0.60$ , and  $+0.90$  [%]; **c** and **d** seven medium-loose ( $e_0 = 0.706$ ) assemblies under  $R = 0.75$  and  $\varepsilon_{v\infty} = -0.90, -0.60, -0.30, 0, +0.30, +0.60$ , and  $+0.90$  [%]; **e** and **f** six medium-loose ( $e_0 = 0.706$ ) assemblies under  $R = 0.05, 0.15, 0.25, 0.35, 0.45$ , and  $0.75$ , and  $\varepsilon_{v\infty} = -0.60$  [%] from  $p'_c = 100$  [kPa]

specimens, and accordingly,  $I_R \approx 1.055$  is obtained prior to shear.  $I_R$  drops below 1.0 in the specimens sheared with  $\zeta = -0.50, -0.25, -0.05, 0.0,$  and  $+0.10$  and these assemblies become hypostatic in shear strains not greater than 0.4 [%]. However, for the specimens sheared under  $\zeta = 0.0$  and  $+0.10$ ,  $I_R$  becomes greater than 1.0 at  $\varepsilon_q \approx 3.7,$  and  $16.3$  [%] following a tangible improvement of CN in Fig. 7e [see blue asterisks in Fig. 18d]. Consequently, the latter specimens become hyperstatic and demonstrate strain hardening subsequent to transient flow instability [see Fig. 7a]. Finally, CN and  $I_R$  improve progressively in specimen sheared under  $\zeta = +0.50$  and therefore, this specimen always remains hyperstatic and no sign of flow instability is observed in its macroscale behavior.

All  $I_R$  versus  $\varepsilon_q$  curves for nine dense assemblies subjected to  $\varepsilon_{v\infty} = -2.50, -1.50, -0.90, -0.60, -0.30, 0, +0.30, +0.60,$  and  $+0.90$  [%] in Fig. 19a drop to reach their minimums around  $\varepsilon_q = 2.3\text{--}3.1$  [%] and then begin to improve with  $\varepsilon_q$  until the critical state. Except for the specimen sheared under  $\varepsilon_{v\infty} = -2.50$  [%],  $I_R$  for the rest of the experiments always remains greater than 1 explaining strong strain hardening in the tests with  $\varepsilon_{v\infty} \geq -1.50$  [%]. The specimen sheared under  $\varepsilon_{v\infty} = -2.50$  [%] becomes hypostatic around  $\varepsilon_q = 1.3$  [%]; however, further shearing results in an increase in CN following a transient minimum and the specimen becomes hyperstatic again around  $\varepsilon_q = 5.7$  [%] {onset of hypo- and hyperstatic regimes are superimposed on stress paths in Fig. 19b}. The mentioned scenario clarifies limited flow instability under transient expansive  $\varepsilon_v\text{--}\varepsilon_1$  coupling with  $\varepsilon_{v\infty} = -2.50$  [%] in Fig. 19a. Similar  $I_R$  versus  $\varepsilon_q$  curves in Fig. 19c for the seven medium-loose particulate assemblies sheared under  $\varepsilon_{v\infty} = -0.90, -0.60, -0.30, 0, +0.30, +0.60,$  and  $+0.90$  [%] (Fig. 9 for the tests) indicate that the increase in the expansive  $\varepsilon_{v\infty}$  accelerates transition from hyperstatic regime to hypostatic regime and causes triggering of the post-peak flow instability at lower shear strengths in the tests sheared under  $\varepsilon_{v\infty} = -0.90, -0.60, -0.30,$  and  $0$  [%].

On the other hand, the increase in the expansive  $\varepsilon_{v\infty}$  postpones the reverse transition from the hypostatic regime to the hyperstatic one and widens the limited flow instability domain. Figure 19d also signifies the certain states for the transition from hyperstatic to hypostatic regime stand slightly after the beginning of the post-peak softening, and the increase in the expansive  $\varepsilon_{v\infty}$  causes a concrete decrease in the stress ratio (i.e.,  $q/p'$ ) at the onset of phase transition from hyperstatic to hypostatic regime. Of note,  $I_R > 0$  holds in the entire shear strain range studied here for the initially medium-loose specimens sheared with  $\varepsilon_{v\infty} = +0.30, +0.60,$  and  $+0.90$  [%] and such systems remain hyperstatic until the end of simulations.

An increase in the pace of expansive volume change (i.e.,  $R$ ) in Fig. 19e, f for six tests sheared under  $\varepsilon_v\text{--}\varepsilon_1$  coupling with  $\varepsilon_{v\infty} = -0.60$  [%] speeds up the decrease in  $I_R$  and  $p'$  leading to faster transition from hyperstatic to hypostatic regime, while delaying reverse transition from hypostatic to hyperstatic regime following phase transformation.

A side-by-side comparison of Figs. 6a, b and 18b indicates that  $I_R = 1$  for the dense ( $e_0 = 0.629$ ) assemblies with  $\zeta = -0.25, -0.50,$  and  $-1.0$  fulfilled at  $\zeta = 0.734, 0.917,$  and  $0.968$ , respectively. Accordingly, the mobilized friction angles at onset of  $I_R = 1$ ,  $\phi'_{I_R=1} = \sin^{-1} \left[ \frac{3\eta}{6+\eta} \right]_{I_R=1}$ , under  $\zeta = -0.25, -0.50,$  and  $-1.0$  become  $19.1^\circ, 23.4^\circ,$  and  $24.6^\circ$ , respectively. A similar practice for the loose ( $e_0 = 0.718$ ) assemblies in Figs. 7 and 18d sheared under  $\zeta = 0, -0.05, -0.25,$  and  $-0.50$  results in  $\eta = 0.412, 0.398, 0.301,$  and  $0.225$  corresponding to  $\phi'_{I_R=1} = 11.1^\circ, 10.7^\circ, 8.2^\circ,$  and  $6.2^\circ$  at the onset of  $I_R = 1$ , respectively. Accordingly, the onset of mechanical instability (i.e.,  $I_R = 1$ ) of the initially dense assemblies sheared under expansive linear  $\varepsilon_v\text{--}\varepsilon_a$  coupling may be triggered at mobilized friction angles more or less greater than the critical state friction angle [i.e.,  $\phi'_{cs} = 20.6^\circ$  (see Sect. 4)] of the assemblies. On the other hand, the mobilized friction angle of the initially loose assemblies at the onset of mechanical instability is significantly lower than  $\phi'_{cs}$ . CN at the onset of  $I_R = 1$  varied in a narrow range from 4.20 to 4.22 for the loose assemblies, whereas it varied 4.13 to 4.29 for the dense ones. In the dense assemblies in Fig. 18b,  $\|dev \mathbf{F}\|$  at  $I_R = 1$  increased from 0.118 to 0.138 owing to the increase in  $\zeta$  from  $-0.25$  to  $-1.0$ ; however, only a negligible change in  $\|dev \mathbf{F}\|$  from 0.035 to 0.015 occurred in the loose assemblies following the increase in  $\zeta$  from zero to  $-0.5$ .

Intensifying expansive  $\varepsilon_v\text{--}\varepsilon_a$  coupling from  $\varepsilon_{v\infty} = 0$  (i.e., constant volume condition) to  $-0.9$  [%] in Figs. 9 and 19d caused  $\phi'_{I_R=1}$  and  $\|dev \mathbf{F}\|$  to decrease from  $15.9^\circ$  to  $12.9^\circ$ , and 0.062 to 0.045, respectively, at the onset of  $I_R = 1$  for the medium-loose assemblies. For the medium-loose assemblies subjected to transient  $\varepsilon_v\text{--}\varepsilon_a$  coupling with  $\varepsilon_{v\infty} = -0.6$  [%] in Figs. 11 and 19f, an increase in  $R$  from 0.05 to 0.75 led to a decrease in  $\phi'_{I_R=1}$  from  $15.7^\circ$  to  $14.0^\circ$ , and decrease in  $\|dev \mathbf{F}\|$  from 0.066 to 0.049 at the onset of  $I_R = 1$ . However, CN  $\approx 4.35$  remained insensitive to change in  $\varepsilon_{v\infty}$  and  $R$  for the experiments in Fig. 19c–f. Analysis of the data mentioned above indicates that expansive transient  $\varepsilon_v\text{--}\varepsilon_a$  coupling may cause mechanical instability earlier than the complete mobilization of  $\phi'_{cs}$  in the loose and medium-loose assemblies.

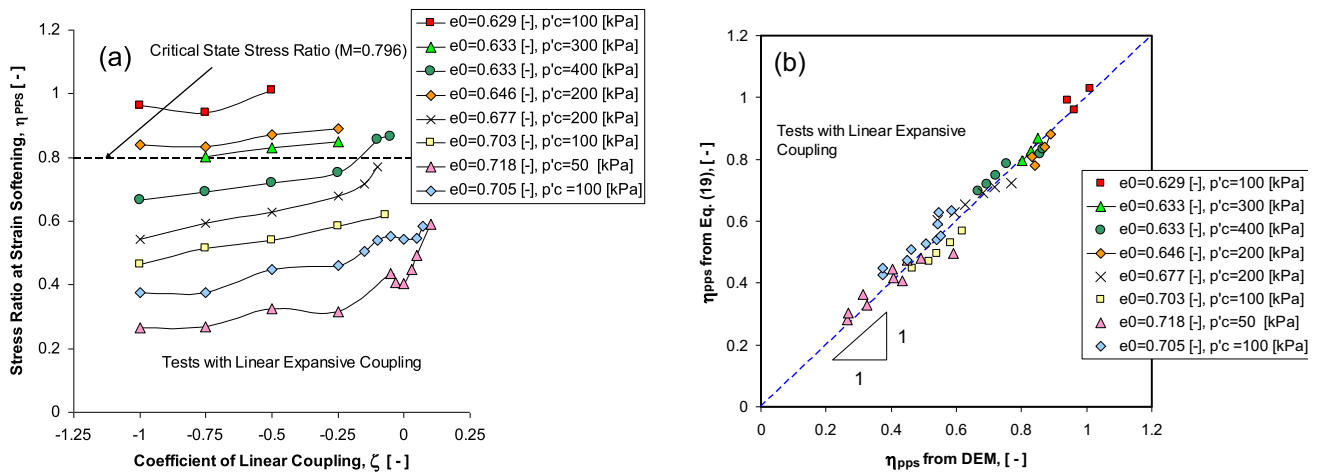


**Fig. 20** Stress ratio at the onset of post-peak strain softening in tests with linear  $\varepsilon_v$ - $\varepsilon_1$  coupling: **a** DEM data, **b** empirical equation prediction versus DEM data

## 6.2 Instability line

Yang [67] has suggested that  $\eta$  at the onset of post-peak softening (i.e.,  $\eta_{PPS}$ ) in undrained TXC tests can be inter-related to  $\psi_0$  (i.e., initial value of  $\psi$ ) through:

$$\eta_{PPS} = A M \exp(B \psi_0) \quad (18)$$

wherein  $A$  ( $< 1$ ) and  $B$  are positive state-dependent sand parameters, and  $M$  is the slope of CSL in the  $q$ - $p'$  plane. Recently, Lashkari et al. [32] showed that Eq. (18) is valid for sands sheared under the constant volume condition in the direct simple shear apparatus. More recently, analysis of the  $\eta_{PPS}$  data obtained from direct simple shear tests with linear coupling between the volumetric and shear strains in Lashkari et al. [30] has revealed that  $A$  in Eq. (18) is not fixed and decreases with  $\zeta$ . In other words, dilatative  $\varepsilon_v$ - $\varepsilon_1$  coupling necessitates lower “ $A$ ” values.

For a total of 51 DEM tests suffering from flow instability under linear  $\varepsilon_v$ - $\varepsilon_1$  coupling, data of stress ratio at the onset of post-peak strain softening (i.e.,  $\eta_{PPS} = q_{PPS}/p'_{PPS}$  wherein  $q_{PPS}$  and  $p'_{PPS}$  are, respectively,  $q$  and  $p'$  at the onset of post-peak strain softening) in Fig. 20a indicate that  $\eta_{PSS}$  decreases with increasing  $p'_c$  and  $e_0$ ; however, the increase in  $\zeta$  and transition from dilatative to contractive coupling yields a tangible rise in  $\eta_{PPS}$ . Figure 20a corroborates that, when the initial state is looser at the beginning (e.g.,  $e_0 \geq 0.677$ ), the greater expansive  $\varepsilon_v$ - $\varepsilon_1$  coupling, achieved through the decrease in  $\zeta$ , or higher confining pressure, results in a lower  $\eta_{PSS}$  (compared to than  $M$ ). This implies that the onset of post-peak softening in loose state is expected to be triggered before the mobilization of  $\phi'_{cs}$ . However, for the initially medium and dense (e.g.,  $e_0 \leq 0.646$ ) assemblies with relatively low values (e.g.,  $p'_c \leq 200$  [kPa]), post-peak softening at stress ratios greater

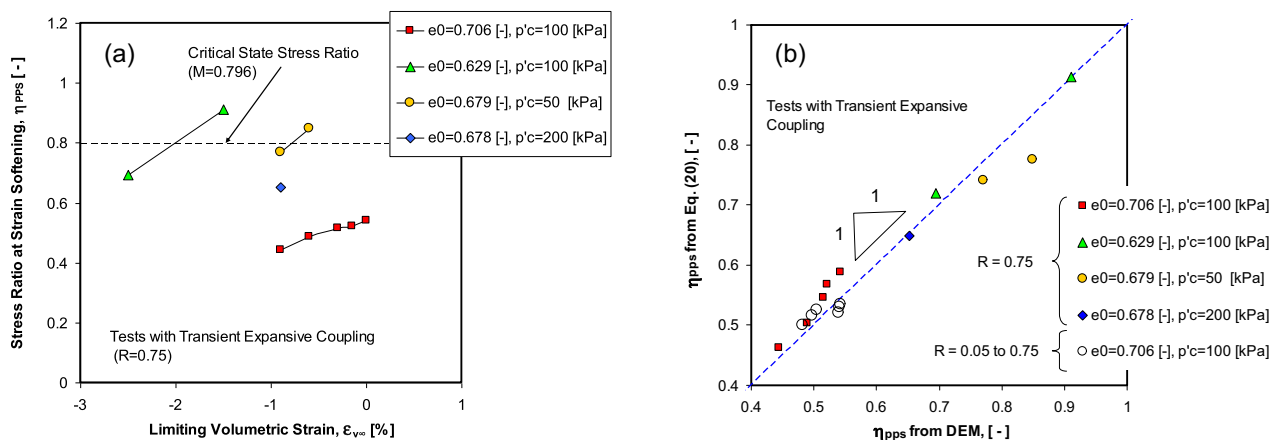


**Fig. 21** Stress ratio at the onset of post-peak strain softening in tests with transient  $\varepsilon_v$ - $\varepsilon_1$  coupling: **a** DEM, **b** empirical equation prediction versus DEM data



than  $M_c$  arises due to linear  $\varepsilon_v-\varepsilon_1$  coupling-induced progressive loosening of the assemblies.

Using the data shown in Fig. 20a, a calibration of Eq. (18) in the following form can link  $\eta_{PPS}$  to  $\zeta$ ,  $e_0$ , and  $\psi_0$  for the virtual DEM experiments with linear  $\varepsilon_v-\varepsilon_1$  coupling:

$$\eta_{PPS} \approx 0.948 \left[ 1 - \left( \frac{e_0}{0.741} \right)^{25.5} + 0.20 \operatorname{sign}(\zeta) |\zeta|^{0.5} \right] M \exp(-5.18 \psi_0) \tag{19}$$

wherein  $B = -5.18$  and

$A = 0.948 \left[ 1 - \left( \frac{e_0}{0.741} \right)^{25.5} + 0.20 \operatorname{sign}(\zeta) |\zeta|^{0.5} \right]$  is a function of  $e_0$  and  $\zeta$ . In Fig. 20b, the predicted  $\eta_{PPS}$  values from Eq. (19) demonstrate a reasonable agreement with the corresponding data from DEM simulations. Similar studies for a total of 20 DEM tests suffering from flow instability under transient  $\varepsilon_v-\varepsilon_1$  coupling with  $R = 0.75$  are presented in Fig. 21a wherein  $\eta_{PPS}$  increases with decreasing  $\varepsilon_{v\infty}$ ,  $e_0$ , and  $\psi_0$ . Compiling the data shown in Fig. 20a together with data of the specimens suffering from flow stability under different R values, the following calibration of Eq. (18) is suggested linking  $\eta_{PPS}$  to  $\varepsilon_{v\infty}$ ,  $R$ ,  $e_0$ , and  $\psi_0$  through:

$$\eta_{PPS} \approx 0.948 \left[ 1 - \left( \frac{e_0}{0.741} \right)^{25.5} + 8.41 \left( \frac{\varepsilon_{v\infty} [\%]}{100 [\%]} \right) (1 + 1.184 R) \right] M \exp(-5.18 \psi_0) \tag{20}$$

wherein  $B = -5.18$  and

$A = 0.948 \left[ 1 - \left( \frac{e_0}{0.741} \right)^{25.5} + 8.41 \left( \frac{\varepsilon_{v\infty} [\%]}{100 [\%]} \right) (1 + 1.184 R) \right]$  is a function of  $e_0$ ,  $\varepsilon_{v\infty}$ , and  $R$ . Of note, Eqs. (19) and (20) predict identical post-peak stress ratio [i.e.,  $\eta_{PPS} \approx 0.948 \left[ 1 - \left( \frac{e_0}{0.741} \right)^{25.5} \right] M \exp(-5.18 \psi_0)$ ] under the constant volume condition wherein  $\zeta = 0$  or  $\varepsilon_{v\infty} = 0$  holds. Predictions obtained from Eq. (20) agree with the DEM data in Fig. 21b.

Figure 22 illustrates a 3D visualization of post-peak softening properties in  $e_{PPS}-\eta_{PPS}-CN$  space under transient coupling conditions. This analysis takes into consideration a wide range of initial void ratios and confining pressures. To enhance the visual clarity of this multidimensional dataset, a color bar is utilized to represent the distance from the  $x$ -axis within the 3D space. In Fig. 22, a direct correlation is observed between  $e_{PPS}$  and  $\eta_{PPS}$ , where an increase in  $e_{PPS}$  corresponds to a decrease in  $\eta_{PPS}$ . This observation highlights that higher initial void ratios are associated with lower stress ratios at the onset of instability. Additionally, post-peak softening is prominently evident for CN values within the range of 4.1 to 5.8.

### 7 Conclusions

The influence of coupling between the volumetric and axial strains on flow instability of the cubic particulate assemblies was investigated in this paper. To this end, a total of 213 DEM simulations (i.e., 24 constant volume, 28 drained, 68 tests with linear  $\varepsilon_v-\varepsilon_1$  coupling, and 93 tests with transient nonlinear  $\varepsilon_v-\varepsilon_1$  coupling) were carried out. The main findings from this study are:

- Loosening of load bearing microstructure during expansive  $\varepsilon_v-\varepsilon_1$  coupling may lead to flow instability of particulate assemblies. It was observed that the decrease in  $\zeta < 0$  (under linear  $\varepsilon_v-\varepsilon_1$  coupling), and decrease in  $\varepsilon_{v\infty} < 0$  and increase in  $R$  (under transient  $\varepsilon_v-\varepsilon_1$  coupling) result in the decrease in peak shear strength, faster post-peak loss of shear strength, rapid accumulation of positive pore-water pressure, quick decrease in CN, and easier evolution of anisotropy in contact force networks.
- Densification of load bearing microstructure under contractive  $\varepsilon_v-\varepsilon_1$  coupling mitigates (or even prevents) the potential of flow instability in particulate assemblies. An increase in  $\zeta > 0$  (under linear coupling) and increases in  $\varepsilon_{v\infty} > 0$  and  $R$  (under transient coupling) cause the increase in peak shear strength, slower post-peak loss of shear strength (if any), slow accumulation of positive pore-water pressure, faster increase in CN, and later evolution of anisotropy.
- Linear  $\varepsilon_v-\varepsilon_1$  coupling prevents particulate specimens from reaching the critical state. No asymptotic values were obtained for CN and  $\|\operatorname{dev} \mathbf{F}\|$  at large shear strains in particulate assemblies shared under linear  $\varepsilon_v-\varepsilon_1$  coupling.
- State of the particulate assemblies sheared under transient  $\varepsilon_v-\varepsilon_1$  coupling approaches the CSL progressively owing to gradual nullification of coupling. For such strain paths, CSL and CN versus  $p'$ , and  $\|\operatorname{dev} \mathbf{F}\|$  versus CN data at the critical state are identical with

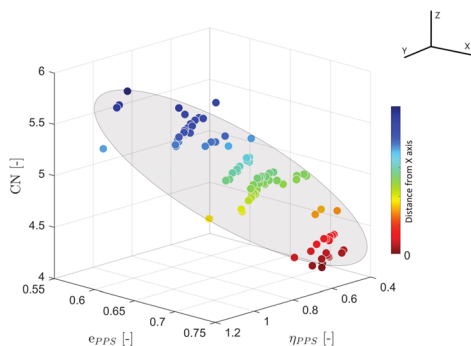


Fig. 22. 3D visualization of post-peak softening properties in  $e_{PPS}-\eta_{PPS}-CN$  space under transient coupling conditions



those of the specimens sheared under the uncoupled paths.

- Flow instability can be investigated by means of sudden jumps in sliding contacts fraction  $f_s$  and redundancy index  $I_R < 1$ . It was observed that  $I_R < 1$  is fulfilled faster with the decrease in  $\zeta < 0$  (in case of dilative linear  $\varepsilon_v - \varepsilon_1$  coupling), decrease in  $\varepsilon_{v\infty} < 0$  and increase in  $R$  (in case of transient dilative  $\varepsilon_v - \varepsilon_1$  coupling). On the other hand, increases in  $\zeta > 0$ ,  $\varepsilon_{v\infty} > 0$  [both leading to contractive  $\varepsilon_v - \varepsilon_1$  coupling] and decrease in  $R$  alleviate flow instability susceptibility through a progressive improvement of  $I_R$  in medium and large shear strains.

**Supplementary Information** The online version contains supplementary material available at <https://doi.org/10.1007/s11440-024-02331-x>.

**Acknowledgements** The authors would like to express their gratitude to Dr. Nazanin Irani for her invaluable assistance during the preparation of the revised version of the manuscript.

**Funding** Open Access funding enabled and organized by Projekt DEAL. The author M. Tafili is grateful to the financial support of the German Research Council (DFG, project No. TR 218/29-1 and No. TA 1696/1-1).

**Data availability** The related data used to support the findings of this study are included within the article and are available from the corresponding author upon reasonable request.

## Declarations

**Conflict of interest** The authors declare that they have no conflict of interest.

**Open Access** This article is licensed under a Creative Commons Attribution 4.0 International License, which permits use, sharing, adaptation, distribution and reproduction in any medium or format, as long as you give appropriate credit to the original author(s) and the source, provide a link to the Creative Commons licence, and indicate if changes were made. The images or other third party material in this article are included in the article's Creative Commons licence, unless indicated otherwise in a credit line to the material. If material is not included in the article's Creative Commons licence and your intended use is not permitted by statutory regulation or exceeds the permitted use, you will need to obtain permission directly from the copyright holder. To view a copy of this licence, visit <http://creativecommons.org/licenses/by/4.0/>.

## References

1. Adamidis O, Madabhushi SPG (2018) Experimental investigation of drainage during earthquake-induced liquefaction. *Geotechnique*. <https://doi.org/10.1680/jgeot.16.P.090>
2. Alipour MJ, Lashkari A (2018) Sand instability under constant shear drained stress path. *Int J Solids Struct*. <https://doi.org/10.1016/j.ijsolstr.2018.06.003>
3. Andrade JE, Ramos AM, Lizcano A (2013) Criterion for flow liquefaction instability. *Acta Geotech*. <https://doi.org/10.1007/s11440-013-0223-x>
4. Azéma E, Radjaï F (2012) Force chains and contact network topology in sheared packings of elongated particles. *Phys Rev E Stat Nonlin Soft Matter Phys*. <https://doi.org/10.1103/PhysRevE.85.031303>
5. Been, Ken, and Mike G. Jefferies. A state parameter for sands. *Geotechnique* 35.2 (1985): 99–112. <https://doi.org/10.1680/geot.1985.35.2.99>
6. Bolton MD (1986) The strength and dilatancy of sands. *Geotechnique*. <https://doi.org/10.1680/geot.1986.36.1.65>
7. Christoffersen J, Mehrabadi MM, Nemat-Nasser S (1981) A micromechanical description of granular material behavior. *J Appl Mech Trans ASME*. <https://doi.org/10.1115/1.3157619>
8. Chu J, Leroueil S, Leong WK (2003) Unstable behaviour of sand and its implication for slope instability. *Can Geotech J*. <https://doi.org/10.1139/t03-039>
9. Chu J, Lo SCR, Lee IK (1992) Strain-softening behavior of granular soil in strain-path testing. *J Geotechn Eng*. [https://doi.org/10.1061/\(ASCE\)0733-9410\(1992\)118:2\(191\)](https://doi.org/10.1061/(ASCE)0733-9410(1992)118:2(191))
10. Chu J, Lo SCR, Lee IK (1993) Instability of granular soils under strain path testing. *J Geotechn Eng*. [https://doi.org/10.1061/\(ASCE\)0733-9410\(1993\)119:5\(874\)](https://doi.org/10.1061/(ASCE)0733-9410(1993)119:5(874))
11. Chu J, Wanatowski D (2008) Instability conditions of loose sand in plane strain. *J Geotechn Geoenviron Eng*. [https://doi.org/10.1061/\(asce\)1090-0241\(2008\)134:1\(136\)](https://doi.org/10.1061/(asce)1090-0241(2008)134:1(136))
12. Cundall PA, Strack ODL (1979) A discrete numerical model for granular assemblies. *Geotechnique*. <https://doi.org/10.1680/geot.1979.29.1.47>
13. Gu X, Huang M, Qian J (2014) DEM investigation on the evolution of microstructure in granular soils under shearing. *Granul Matter*. <https://doi.org/10.1007/s10035-013-0467-z>
14. Guo N, Zhao J (2013) The signature of shear-induced anisotropy in granular media. *Comput Geotech*. <https://doi.org/10.1016/j.compgeo.2012.07.002>
15. Hosseininia ES (2013) Stress-force-fabric relationship for planar granular materials. *Geotechnique*. <https://doi.org/10.1680/geot.12.P.055>
16. Hu Z, Yang ZX, Zhang YD (2020) CFD-DEM modeling of suffusion effect on undrained behavior of internally unstable soils. *Comput Geotech*. <https://doi.org/10.1016/j.compgeo.2020.103692>
17. Huang X, Yee KC, Hanley KJ, Zhang Z (2018) DEM analysis of the onset of flow deformation of sands: linking monotonic and cyclic undrained behaviours. *Acta Geotech*. <https://doi.org/10.1007/s11440-018-0664-3>
18. Irani N, Lashkari A, Tafili M, Wichtmann T (2022) A state-dependent hyperelastic-plastic constitutive model considering shear-induced particle breakage in granular soils. *Acta Geotech* 17(11):5275–5298. <https://doi.org/10.1007/s11440-022-01636-z>
19. Irani N, Ghasemi M (2021) Effect of scrap tyre on strength properties of untreated and lime-treated clayey sand. *Eur J Environ Civ Eng* 25(9):1609–1626. <https://doi.org/10.1080/19648189.2019.1585964>
20. Ishihara K (1993) Liquefaction and flow failure during earthquakes. *Geotechnique*. <https://doi.org/10.1680/geot.1993.43.3.351>
21. Itasca Consulting Group Inc (2014) Particle flow Code in three-dimensions user's manual, Version. 5.0. Minneapolis: Itasca
22. Iwashita K, Oda M (1999) Mechanics of Granular materials: an introduction. In: fundamentals for mechanics of granular material. <https://doi.org/10.1201/9781003077817>
23. Jiang M, Zhang A, Fu C (2018) 3-D DEM simulations of drained triaxial tests on inherently anisotropic granulates. *Eur J Environ Civ Eng*. <https://doi.org/10.1080/19648189.2017.1385541>
24. Jrad M, Sukumaran B, Daouadji A (2012) Experimental analyses of the behaviour of saturated granular materials during

- axisymmetric proportional strain paths. *Eur J Environ Civil Eng.* <https://doi.org/10.1080/19648189.2012.666900>
25. Kamai R, Boulanger RW (2012) Single-element simulations of partial-drainage effects under monotonic and cyclic loading. *Soil Dyn Earthq Eng.* <https://doi.org/10.1016/j.soildyn.2011.10.002>
  26. Ken-Ichi K (1984) Distribution of directional data and fabric tensors. *Int J Eng Sci.* [https://doi.org/10.1016/0020-7225\(84\)90090-9](https://doi.org/10.1016/0020-7225(84)90090-9)
  27. Khabazian M, Hosseinia ES (2020) Instability of saturated granular materials in biaxial loading with polygonal particles using discrete element Method (DEM). *Powder Technol.* <https://doi.org/10.1016/j.powtec.2020.01.013>
  28. Kruyt NP, Rothenburg L (2009) Plasticity of granular materials: a structural-mechanics view. In: AIP conference proceedings. <https://doi.org/10.1063/1.3179830>
  29. Lade PV, Nelson RB, Ito YM (1988) Instability of granular materials with nonassociated flow. *J Eng Mech.* [https://doi.org/10.1061/\(asce\)0733-9399\(1988\)114:12\(2173\)](https://doi.org/10.1061/(asce)0733-9399(1988)114:12(2173))
  30. Lashkari A, Falsafizadeh SR, Rahman MM (2021) Influence of linear coupling between volumetric and shear strains on instability and post-peak softening of sand in direct simple shear tests. *Acta Geotech.* <https://doi.org/10.1007/s11440-021-01288-5>
  31. Lashkari A, Shourijeh PT, Khorasani SS, Irani N, Rahman MM (2022) Effects of over-consolidation history on flow instability of clean and silty sands. *Acta Geotech* 17(11):4989–5007
  32. Lashkari A, Falsafizadeh SR, Shourijeh PT, Alipour MJ (2020) Instability of loose sand in constant volume direct simple shear tests in relation to particle shape. *Acta Geotech.* <https://doi.org/10.1007/s11440-019-00909-4>
  33. Lashkari A, Yaghtin MS (2018) Sand flow liquefaction instability under shear–volume coupled strain paths. *Geotechnique.* <https://doi.org/10.1680/jgeot.17.P.164>
  34. Lashkari A, Khodadadi M, Binesh SM, Rahman MDM (2019) Instability of particulate assemblies under constant shear drained stress path: DEM approach. *Int J Geomech.* [https://doi.org/10.1061/\(asce\)gm.1943-5622.0001407](https://doi.org/10.1061/(asce)gm.1943-5622.0001407)
  35. Li XS, Dafalias YF (2000) Dilatancy for cohesionless soils. *Geotechnique.* <https://doi.org/10.1680/geot.2000.50.4.449>
  36. Li XS, Wang Y (1998) Linear representation of steady-state line for sand. *J Geotech Geoenviron Eng.* [https://doi.org/10.1061/\(asce\)1090-0241\(1998\)124:12\(1215\)](https://doi.org/10.1061/(asce)1090-0241(1998)124:12(1215))
  37. Li X, Yu HS, Li XS (2009) Macro-micro relations in granular mechanics. *Int J Solids Struct.* <https://doi.org/10.1016/j.ijsolstr.2009.08.018>
  38. Li X, Yu HS (2009) Influence of loading direction on the behavior of anisotropic granular materials. *Int J Eng Sci.* <https://doi.org/10.1016/j.jengsci.2009.03.001>
  39. Li XS, Dafalias YF (2012) Anisotropic critical state theory: role of fabric. *J Eng Mech.* [https://doi.org/10.1061/\(ASCE\)EM.1943-7889.0000324](https://doi.org/10.1061/(ASCE)EM.1943-7889.0000324)
  40. Liu J, Zhou W, Ma G, Yang S, Chang X (2020) Strong contacts, connectivity and fabric anisotropy in granular materials: a 3D perspective. *Powder Technol.* <https://doi.org/10.1016/j.powtec.2020.03.018>
  41. Malvick EJ, Kulasingam R, Kutter BL, Boulanger RW (2022) Void redistribution and localized shear strains in slopes during liquefaction. In: *Physical modelling in geotechnics.* <https://doi.org/10.1201/9780203743362>
  42. Mehrabadi MM, Nemat-Nasser S, Oda M (1982) On statistical description of stress and fabric in granular materials. *Int J Numer Anal Methods Geomech.* <https://doi.org/10.1002/nag.1610060107>
  43. Nguyen HBK, Rahman MM, Fourie AB (2018) Characteristic behavior of drained and undrained triaxial compression tests: DEM study. *J Geotech Geoenviron Eng.* [https://doi.org/10.1061/\(asce\)gt.1943-5606.0001940](https://doi.org/10.1061/(asce)gt.1943-5606.0001940)
  44. Nguyen HBK, Rahman MM, Fourie AB (2017) Undrained behaviour of granular material and the role of fabric in isotropic and K0 consolidations: DEM approach. *Geotechnique.* <https://doi.org/10.1680/jgeot.15.P.234>
  45. Nicot F, Daouadji A, Hadda N, Jrad M, Darve F (2013) Granular media failure along triaxial proportional strain paths. *Eur J Environ Civil Eng.* <https://doi.org/10.1080/19648189.2013.819301>
  46. Nicot F, Darve F (2011) Diffuse and localized failure modes: two competing mechanisms. *Int J Numer Anal Methods Geomech.* <https://doi.org/10.1002/nag.912>
  47. Roscoe KH, Schofield AN, Wroth CP (1958) On the yielding of soils. *Geotechnique.* <https://doi.org/10.1680/geot.1958.8.1.22>
  48. Rothenburg L, Bathurst RJ (1990) Discussion: analytical study of induced anisotropy in idealized granular material. *Géotechnique.* <https://doi.org/10.1680/geot.1990.40.4.665>
  49. Rowe P (1962) The stress-dilatancy relation for static equilibrium of an assembly of particles in contact. *Proc R Soc Lond A Math Phys Sci.* <https://doi.org/10.1098/rspa.1962.0193>
  50. Salimi MJ, Lashkari A (2020) Undrained true triaxial response of initially anisotropic particulate assemblies using CFM-DEM. *Comput Geotech* 124:103509. <https://doi.org/10.1016/j.compgeo.2020.103509>
  51. Salimi M, Tafili M, Irani N, Wichtmann T (2023) Micro-mechanical response of transversely isotropic samples under cyclic loading. In: *10th European conference on numerical methods in geotechnical engineering.* <https://doi.org/10.53243/NUMGE2023-179>
  52. Satake M (1982) Fabric tensor in granular materials. Deformation and failure of granular materials IUTAM symposium, Delft
  53. Seyedi HE (2015) A micromechanical study on the stress rotation in granular materials due to fabric evolution. *Powder Technol.* <https://doi.org/10.1016/j.powtec.2015.06.013>
  54. Seyedi HE (2012) Discrete element modeling of inherently anisotropic granular assemblies with polygonal particles. *Particuology.* <https://doi.org/10.1016/j.partic.2011.11.015>
  55. Shi J, Guo P (2018) Fabric evolution of granular materials along imposed stress paths. *Acta Geotech.* <https://doi.org/10.1007/s11440-018-0665-2>
  56. Sivathayalan S, Logeswaran P (2008) Experimental assessment of the response of sands under shear-volume coupled deformation. *Can Geotech J.* <https://doi.org/10.1139/T08-068>
  57. Sladen JA, D'Hollander RD, Krahn J (1985) The liquefaction of sands, a collapse surface approach. *Can Geotech J.* <https://doi.org/10.1139/t85-076>
  58. Sufian A, Russell AR, Whittle AJ (2017) Anisotropy of contact networks in granular media and its influence on mobilised internal friction. *Geotechnique.* <https://doi.org/10.1680/jgeot.16.P.170>
  59. Suzuki Y, Carotenuto P, Dyvik R, Jostad HP (2020) Experimental study of modeling partially drained dense sand behavior in monotonic triaxial compression loading tests. *Geotech Test J* 43(5):1174–1190
  60. Tafili M, Grandas Tavera C, Triantafyllidis T, Wichtmann T (2021) On the dilatancy of fine-grained soils. *Geotechnics* 1(1):192–215
  61. Tafili M, Triantafyllidis T (2019). State-dependent dilatancy of soils: experimental evidence and constitutive modeling. In: *Recent developments of soil mechanics and geotechnics in theory and practice*, Springer International Publishing, Cham, pp 54–84
  62. Vaid YP, Eliadorani A (2000) Undrained and drained (?) stress-strain response. *Can Geotech J.* <https://doi.org/10.1139/t00-036>
  63. Wan RG, Guo PJ (1998) A simple constitutive model for granular soils: modified stress-dilatancy approach. *Comput Geotech.* [https://doi.org/10.1016/S0266-352X\(98\)00004-4](https://doi.org/10.1016/S0266-352X(98)00004-4)

64. Wichtmann T, Triantafyllidis T (2016) An experimental database for the development, calibration and verification of constitutive models for sand with focus to cyclic loading: part I—tests with monotonic loading and stress cycles. *Acta Geotech*. <https://doi.org/10.1007/s11440-015-0402-z>
65. Wu QX, Xu TT, Yang ZX (2020) Diffuse instability of granular material under various drainage conditions: discrete element simulation and constitutive modeling. *Acta Geotech*. <https://doi.org/10.1007/s11440-019-00885-9>
66. Yamamoto Y, Hyodo M, Orense RP (2009) Liquefaction resistance of sandy soils under partially drained condition. *J Geotechn Geoenviron Eng*. [https://doi.org/10.1061/\(asce\)gt.1943-5606.0000051](https://doi.org/10.1061/(asce)gt.1943-5606.0000051)
67. Yang ZX, Wu Y (2017) Critical state for anisotropic granular materials: a discrete element perspective. *Int J Geomech*. [https://doi.org/10.1061/\(asce\)gm.1943-5622.0000720](https://doi.org/10.1061/(asce)gm.1943-5622.0000720)
68. Yegian MK, Eseller-Bayat E, Alshawabkeh AS, Ali S (2007) Induced-partial saturation for liquefaction mitigation: experimental investigation. *J Geotech Geoenviron Eng* 133(4):372–380
69. Yoshimine M, Ishihara K, Vargas W (1998) Effects of principal stress direction and intermediate principal stress on undrained shear behavior of sand. *Soils Found*. [https://doi.org/10.3208/sandf.38.3\\_179](https://doi.org/10.3208/sandf.38.3_179)
70. Zhao J, Guo N (2013) Unique critical state characteristics in granular media considering fabric anisotropy. *Geotechnique*. <https://doi.org/10.1680/geot.12.P.040>
71. Zhou W, Liu J, Ma G, Chang X (2017) Three-dimensional DEM investigation of critical state and dilatancy behaviors of granular materials. *Acta Geotech*. <https://doi.org/10.1007/s11440-017-0530-8>

**Publisher's Note** Springer Nature remains neutral with regard to jurisdictional claims in published maps and institutional affiliations.